
Long-term optical imaging of the spinal cord in awake behaving mice

In the format provided by the authors and unedited

This PDF file includes the following:

SUPPLEMENTARY NOTES	3
Supplementary Note 1 <i>In vivo</i> spinal cord preparations for longitudinal imaging	3
Supplementary Note 2 Surgical considerations for chamber implant and assembly	5
Supplementary Note 3 Fibrosis inhibition with fluoropolymers	6
Supplementary Note 4 Post-operative recovery	8
Supplementary Note 5 Customized surgical table, equipment and materials	9
Supplementary Note 6 Machining and fabrication of the spinal chamber	10
Supplementary Note 7 Considerations and setups for <i>in vivo</i> spinal cord imaging	11
Supplementary Note 8 Optimizing <i>in vivo</i> spinal cord imaging: cameras and objectives	12
Supplementary Note 9 Optimizing <i>in vivo</i> spinal cord imaging: reducing photodamage	13
Supplementary Note 10 Processing, display, and 3D rendering of microCT data	14
Supplementary Note 11 Additional details of the rotarod assay	15
Supplementary Note 12 Body part annotation during behavior video analysis	16
Supplementary Note 13 Feature selection for accurate LD-MCM motion correction	17
Supplementary Note 14 Cross-session fluorescence intensity normalization methods	18
SUPPLEMENTARY FIGURES	19
Supplementary Fig. 1 Key frames of the first procedure - Chamber implantation	19
Supplementary Fig. 2 Key frames of the second procedure - Laminectomy	20
Supplementary Fig. 3 Key frames of the third procedure - Spinal cord window placement	21
Supplementary Fig. 4 Histological analysis post chamber implant and laminectomy	22
Supplementary Fig. 5 Long-term imaging of axons in the spinal cord of awake mice	23
Supplementary Fig. 6 Imaging of spinal cord neuronal activity in anesthetized animals	24
Supplementary Fig. 7 Multiplane two-photon imaging of CX3CR1-EGFP mouse	25
SUPPLEMENTARY TABLES	26
Supplementary Table 1 Chamber implant step-by-step	26
Supplementary Table 2 Laminectomy step-by-step	28
Supplementary Table 3 Window placement step-by-step	29
Supplementary Table 4 Materials used for <i>in vivo</i> imaging of the mouse spinal cord	30
SUPPLEMENTARY REFERENCES	35

SUPPLEMENTARY NOTES

Supplementary Note 1 | *In vivo* spinal cord preparations for longitudinal imaging

Here we provide an overview of the pioneering and more recent techniques developed to enable longitudinal optical access to the spinal cord and compare their approaches to our end-to-end pipeline. To summarize, many prior studies conducted longitudinal spinal cord imaging under repeated anesthesia and more recent publications demonstrated awake recordings, often with a more limited duration of imaging. Further, with the exception of a single recent study, no others demonstrated large bilateral field of view imaging in the spinal cord of awake animals and none did consistently over time. Several studies achieved longitudinal imaging either by 1) covering the spinal cord with a protective material that was removed before each imaging session or 2) reparation of the spinal chamber window after onset of fibrosis. Reparation involves removing the glass coverslip to manually remove any regrowth before replacing the window and resuming imaging. Both these approaches are less ideal from an animal health, experimental, and scientific perspective and preclude certain experiments. Further, repeated anesthesia raises concerns about animal welfare and potential scientific confounds (e.g. isoflurane alters the proteome); and one study reported limiting collection of certain time points due to animal care restrictions. Several studies noted surgical methods to reduce motion—e.g. pressing the cover glass close to the spinal cord (which has been noted to cause inflammation and other issues) or using specific anesthetics (e.g. urethane over ketamine, xylazine, and acepromazine). Lastly, more recent studies that conducted awake spinal cord imaging often lack longitudinal imaging data or have a limited field of view.

We solve many of these issues (**Extended Data Fig. 1a**). We conduct an initial set of surgeries using an easily manufactured and assembled spinal chamber followed by long-term, bilateral imaging of the spinal cord in awake, behaving mice, via rapid mounting as we demonstrate here for spinally-fixed (**Fig. 3a**) or freely moving (**Fig. 4l-o**, **Extended Data Fig. 9e-q**) animals. While others noted issues of chamber stability over time or after repeated imaging, we solved this issue with spinous process needles (**Fig. 1a, e**) and blinders (**Fig. 4c**). Further, we developed and characterized a motion correction workflow to handle the variety and extent of spinal cord motion seen (**Fig. 2**). Lastly, our objective is to image the dorsal horn grey matter, which is often first affected by fibrosis due to it being greater than ~300 μm lateral to the midline dorsal vein and nearer to the laminectomy incision sites where fibrosis originates. This arrangement contrasts with studies, such as Farrar, 2012, that imaged axons that predominantly course through the medial white matter and are often affected last by regrowth. Thus, improved fibrosis inhibition with Teflon AF allows long-term imaging of the grey matter (**Fig. 1f-g**), critical for longitudinal neural activity analysis.

Pioneering work attempted to establish electrophysiological recording in awake, behaving rats¹, cats², and mice³. However, optical imaging has several advantages, including studying morphology and spatial dynamics of neurons, glia, and other cells. Early spinal cord imaging studies performed anesthetized recordings and performed repeated imaging via placement of a protective layer over the spinal cord followed by suturing of the overlying tissue, such as muscles and skin⁴⁻⁷. These protective materials were then repeatedly removed during each day of imaging, enabling several imaging sessions for days to several months, depending on the preparation; however, at times, this involved several month gaps between sessions. Subsequent studies followed these procedures, such as Lorenzana, 2015⁸ imaging at 5 days, 5 weeks, and 6 months using the reopening method described in Davalos, 2008—indicating that imaging at 6 months using this method is unlikely without reparation.

A series of papers established longitudinal imaging through permanent optical windows in anesthetized animals, by covering the exposed cord with biocompatible silicone adhesives (e.g. Kwik-Sil) but used different designs for the spinal chambers⁹⁻¹¹. This enabled Farrar, 2012 to image for weeks to months, but the number of usable animals varied from ~50–75% at 5 weeks—this is in contrast to our clarity of ~75% animals at ~90 days (**Fig. 1g**). The spinal chamber introduced in Farrar, 2012 has subsequently been used numerous times. Fenrich, 2012 noted that light anesthesia was used to minimize physical stress associated with restraining the animal—an issue we solved with spinous process needles (**Fig. 1a, e**) and blinders (**Fig. 4c**). Figley, 2013 reported reparation at 21 days to extend imaging and their chambers often detached after 29 days due to suture failure—neither of which we have to do nor see in our preparation. Several studies built on this work, such as a series of spinal cord injury studies imaging for 2–3 days¹²⁻¹⁵ or the Debarbieux lab imaging up to 90 days^{16,17}.

Despite these advances, fibrosis and repeated anesthesia remain an issue. Farrar, 2014 noted that they see “dense fibrous overgrowth” that obscures the FOV as early as three days¹⁸. DeNotta, 2018 described the visibility of imaging chambers remaining clear for approximately 1–2 weeks, after which a pale pink

haze emerged that was attributed to fibrinous granulation tissues and eventual fibrous scarring¹⁹. These findings match our observations using Kwik-Sil only (**Fig. 1f-g**). Laskowski, 2013 noted that lesions for SCI studies induce fibrosis²⁰. Cupido, 2014 used the Fenrich, 2012 method to image microglia but did not specifically report the length of time they could image from individual animals²¹. Cartarozzi, 2018 developed an approach to image the ventral horn based on the work in the Kirchhoff group and are able to image for hours, but they explicitly state that longitudinal imaging is not possible²²⁻²⁴. Shekhtmeyster, 2019 reported that surgical preparations in the lab would at times have to be redone and that the Farrar, 2012 preparation would produce pressure that led to inflammation and reduced ability to record normal cellular activity²⁵. This pressure is in part used to minimize spinal cord motion, which we address (**Fig. 2**). Rajaei, 2020 followed mice for up to 14 days; however, they report that scar formation limited imaging and, along with the need to perform repeated anesthesia, prevented imaging of all animals at all time points desired²⁶. By imaging the intervertebral space after application of Iodixanol (OptiPrep), Wu, 2022 attempted to circumvent the issues with laminectomy; however, they require a reopening procedure before each imaging session, which sometimes included reoperation, along with supplementing Iodixanol during imaging due to washout. Sullivan, 2022 showed the effects of increased isoflurane concentration on vGluT2 and vAAT neurons along with characterizing their responses to mechanical and thermal stimuli. They mentioned having to reprepare the spinal cord and did not demonstrate cross-session imaging²⁷. Rieder, 2022 and Rieder, 2023 reported imaging of astrocytes and microglia for up to 7 days in chronic window preparations using isoflurane anesthesia (based on Cupido, 2014) during imaging^{28,29}. Yarmolinsky, 2024 recently demonstrated long-term imaging of neurons in anesthetized animals before and after injury; however, they used a subset of fibrosis-free animals as they note that³⁰ “spinal windows frequently exhibit a degraded clarity within the first post-surgical week due to neovascularization and fibrosis over the imaging area”. Taken together, even recent work highlights the need for consistent ability to maintain long-term optical clarity during spinal cord imaging.

More recently, a number of studies have conducted imaging in awake animals using miniature microscopes or two-photon microscopy³¹⁻³⁵. Sekiguchi, 2016 demonstrated an example recording of neural activity from one mouse 6 days after surgery under isoflurane anesthesia, but otherwise performed surgery and imaging on the same day. Shekhtmeyster, 2023a reported imaging mice either immediately or 4–7 days after window placement and mentioned needing to at times conduct reoperation before imaging. Shekhtmeyster, 2023b reported imaging up to four weeks; however, no longitudinal data were presented and they used a microprism implanted directly into the spinal cord. Cheng, 2016 report observing GCaMP6 expression two weeks after injection and chamber placement while recording in awake, behaving spinally fixed animals, but showed no longitudinal data³⁴. Ju, 2022 adapted the design of Farrar, 2012 to conduct miniature microscope two-photon imaging in freely moving animals, albeit with a 420×420 μm^2 field of view restricted to one side of the spinal cord, and report imaging up to 60 days without quantifying imaging quality³⁵. Celinskis, 2022 noted that they could image up to 37 days before overgrowth or fibrosis precluded optical access (as they noted, “the dominant form of spinal cord implant failure”) and mentioned the need for a systematic method of comparing different fibrosis inhibiting methods³⁶, which we have demonstrated here using Kaplan-Meier curve analysis to compare Kwik-Sil only to PRECLUDE + Teflon AF (**Fig. 1g**) and agree these types of analyses will be important for the field going forward. Celinskis, 2023 further corroborated their initial observations³⁷.

This overview demonstrates the many significant advances made to image the spinal cord, but also highlights several limitations encountered previously. Here we addressed these limitations with our spinal cord preparation, setup, and computational analysis (**Extended Data Fig. 1a**). Further, the common use of silicone adhesives highlights how our use of an optically transparent fluoropolymer (Teflon AF 2400), which inhibits fibrosis for months to over a year, can lead the field to investigate additional optically transparent biocompatible materials that can inhibit fibrosis and improve the ability to record in awake, behaving animals.

Supplementary Note 2 | Surgical considerations for chamber implant and assembly

The side bar position will vary slightly for each mouse, so the freedom of movement of the side bars greatly facilitates the positioning of the chamber during surgery. To adjust the width of the metal chamber, instead of using small metal screws that are difficult to handle, we use Super Glue to attach the metal parts. Metal surfaces covered with Super Glue are then clamped together setting a strong bond, which obviates the need for set screws. Surgifoam® is used in the first procedure for hemostasis and protection of the intervertebral tissue, before Kwik-Sil. To keep the tissue hydrated, saline-soaked Surgifoam pieces are placed in intervertebral areas and in rostral and caudal areas of open tissue, until the bars are in place. After the bars are in position, the Surgifoam is removed and the space is briefly dried with a sponge. Small drops of Kwik-Sil are then applied to cover the intervertebral space; these sit at room temperature until cured. The Kwik-Sil mask is maintained throughout cementing steps. Critically, the mask protects intervertebral space from the dentin activator and liquid cement, which are applied in bulk to free-flow around the mask. An unprotected intervertebral space is vulnerable to chemical and mechanical injury, which will not only create significant bleeding, but also lead to permanent damage to the spinal meninges and spinal cord.

The needles that are inserted perpendicular to the spinal column, through the dorsal spinous processes (DSP), are a key step and allow the components to be constructed around the vertebrae. We use a 33G needle (Accuderm, NP335) with a beveled edge and a bore size diameter of 0.2 mm. Place the needle on a 1-mL syringe and rotate the cutting edge to facilitate driving it through the DSP bone. When the needle is through, snip the needle at the base of the shaft to have equal lengths of the needle on each side.

Extended Data Fig. 2a-i illustrates the cross-sectional anatomy of a vertebra and the location of the dorsal spinous process, facet joints, and lamina, and how the side bars are positioned relative to these vertebral landmarks. Note that only the facet joints surrounding the middle vertebrae (T13) are exposed during surgery. Before cement application, it is important to debride any tissue above the vertebral bone as this tissue could come into contact with the cement. To further improve the bone cement (PMMA) connection to the bone, a pretreatment with a dentin activator (included in Metabond kit) is recommended. Of course, any cement placed on soft tissue or ill-prepared bone will not hold, as can happen when blood debris sticks to the bone. Before installing the stabilizing plate, gently press down the middle vertebrae and carefully lower both side bars, so that the alignment between vertebrae is as flat as possible before fixation.

Supplementary Note 3 | Fibrosis inhibition with fluoropolymers

In previous spinal cord optical imaging methods⁹, post-laminectomy fibrosis was abated by room-temperature vulcanizing (RTV) silicone adhesive, namely, Kwik-Sil, applied directly over the spinal cord. However, we found that significant regrowth occurs under a bare Kwik-Sil or a pre-cured Polydimethylsiloxane (PDMS) layer. Therefore, we adopted two fluoropolymer materials: GORE® PRECLUDE® Pericardial Membrane (a form of expanded polytetrafluoroethylene [ePTFE]) and Teflon™ AF (an amorphous fluoropolymer film).

Teflon AF and ePTFE are materials derived from polytetrafluoroethylene (PTFE) and licensed by Chemours Company FC, LLC under the brand Teflon™. Both materials exhibit PTFE's durability and chemical resistance characteristics. However, the structural characteristics of each are notably different. ePTFE is a form of PTFE that has been expanded, resulting in a network of nodes and fibrils, making it highly porous and lightweight, appearing white and spongy. ePTFE is commonly used in medical implants³⁸. The porosity size of ePTFE is a determinant of tissue integration, with larger pore sizes allowing tissue integration, which can be beneficial after some surgical procedures. However, ingrowth of cells is impossible at the <1- μ m pore size of the ePTFE formulation (PRECLUDE membrane, Gore Medical) used in this study (**Extended Data Fig. 2j**). In contrast to the mechanically-based fabrication that produces ePTFE, Perfluoro-(2,2-dimethyl-1,3-dioxole) (Teflon AF) is produced by adding a chemical comonomer to TFE so that the structure is unable to crystallize, characterizing this material as an amorphous fluoropolymer³⁹. Due to its amorphous nature, Teflon AF can be formed into thin films or coatings that are optically transparent. Teflon AF stands out in terms of its high gas permeability, low dielectric constant, and low refractive index [RI]. This RI is claimed to be the lowest of any known fluoroplastic or solid organic polymer⁴⁰.

As mentioned above, medical grade ePTFE is approved for implantation into the human body, such as vascular stents and endoprosthesis (see <https://www.goremedical.com/products>). ePTFE materials are intrinsically durable in the body because they resist hydrolysis due to their highly hydrophobic properties. Importantly, ePTFE, alongside other dura plastic materials, can serve as a dural substitute. Medical literature describing reoperations in recurrent low-grade gliomas (LGG) highlights the absence of tissue attachment and fibrosis during reoperation, reducing surgery time and complications⁴¹. There are also reports of ePTFE's effectiveness in preventing postoperative peridural fibrosis^{42,43}. Similarly, surgically implanted PRECLUDE® Pericardial membranes, the form used here, develop few to no adhesions, allowing the material's quick removal and an overall decrease in time of cardiovascular surgery at reoperation^{44,45}.

Hydrophilic properties, such as wettability and resistance to proteinaceous deposits, are sometimes introduced along the surface of bulk hydrophobic materials, improving biocompatibility. On a mechanistic basis, one theory is that a layer of intermediate water forms adjacent to the inert fluoropolymer membrane in the body, which prevents molecules from interacting with the membrane⁴⁶. Hydrophilic coatings in this way would facilitate this layer and thus limit protein deposits. Interestingly, a hydrophilic coating of the PRECLUDE membrane was not necessary for post-laminectomy fibrosis inhibition. A key variable is likely due to ePTFE's porosity (**Extended Data Fig. 2j**). Porosity is a crucial attribute frequently utilized in implants and tissue scaffolds⁴⁷. In contrast, Teflon AF, which is non-porous (**Extended Data Fig. 2k**), did not display adequate regrowth inhibition when placed immediately after laminectomy. Thus, a molecular coating of hydrophilic units may improve the post-laminectomy compatibility, similar to another amorphous fluoropolymer, CYTOP, and its successful interface with the brain meninges after PEO-coating^{48,49}. However, the low surface energy—characteristic of PTFE-based fluoropolymers—makes it challenging to apply a hydrophilic coating. For example, the protocol to coat CYTOP with PEO subunits presented by Takahashi, 2020⁴⁸ requires equipment to spin-cast fluoropolymers onto a silicon wafer, to introduce PEO units to the surface of the fluoropolymer, and then to surface-treat with oxygen plasma followed by performing surface element analysis for quality control. Alternatively, one can order PRECLUDE and Teflon AF commercially.

In summary, the outstanding hydrophobic, low surface energy, and no nonspecific absorption properties of ePTFE and Teflon AF contribute to chronic biocompatibility without tissue integration. The overarching theory is that these forms of Teflon are biologically inert materials that can prevent mechanical contact between meningeal layers and connective tissue for an extended time and thus allow independent healing of the meningeal surface⁵⁰. When ePTFE (PRECLUDE) and subsequently Teflon AF are added to the laminectomized area, an effective barrier agent above the spinal cord is formed and fibrosis is marginalized

to locations that do not interfere with imaging. This mechanism has also been suggested to enable cranial imaging studies^{51–53}. Other materials, namely polyethylene terephthalate (PET) film, used in brain imaging protocols, and other fluoropolymers—Teflon FEP (Fluorinated Ethylene Propylene) or Teflon PFA (perfluoroalkoxy)—may play a similar role as Teflon AF. However, they remain untested as agents that could preserve spinal visibility⁵⁴. In future studies, it is possible that reducing the thickness of the Teflon AF to a nanosheet would adhere more tightly to the spinal cord than the thicker membranes used in this study. Though nanosheet handling is difficult, fluoropolymer nanosheets of 130 nm thickness, namely CYTOP, have proven sufficient for long-term cranial imaging⁴⁸. Interestingly, as nanosheets are penetrable, it may be possible to permit electrode manipulation, optical recording, and chronic micro-injections in a stable state of fibrosis inhibition.

Supplementary Note 4 | Post-operative recovery

Robust recovery after chamber implant

The animals are fully mobile after surgery. At 24 hrs, the animals are somewhat limited in their speed of movement but are alert, ambulate, and groom. By 48 hrs, the animals spontaneously rear and show normal movements. For the first cohort of spinally-implanted mice, we recommend that labs conduct behavioral and sensory testing to ensure that implants are not altering animal state.

Implant location considerations

Placing side bars under the facet joints surrounding the middle vertebra of interest (along with the dorsal spinous process needles on the flanking vertebrae) can theoretically be attempted at any triplet of vertebrae along the spine. For instance, we were able to successfully image the L6/S1 spinal cord by a T13-L2 side bar placement and L1 laminectomy (**Fig. 4i-k**). However, L1 animals commonly presented with severe urinary retention and succumbed 48-72 hours after surgery. We have not explored whether other rostrocaudal positions are possible. Post-op excretion of urine through manual compression at 24 hours, under anesthesia, was necessary for survival in cases associated with L1 surgery. In some cases, there were post-op complications with a slow-release form of Buprenorphine, namely, Ethiq.

Cutaneous self-injury

Occasionally chemical or mechanical intervertebral injury during surgery can produce a focal, but treatable, problem. The animals will show focal skin lesions due to self-inflicted biting. These can be treated with a three-day regimen of Chlorhexidine and triple antibiotic ointment, but ultimately depends on lab and institutional existing protocols for such injuries. For the T13-centered implant, which overlies the L4/L5 spinal cord segments, biting occasionally occurred in the L4/L5 dermatome, including the hindpaw. Attention to the intraoperative, intervertebral mask using Kwik-Sil, will prevent the potential toxicity of liquid dentin activator (ferric chloride) or uncured cement (PMMA).

Supplementary Note 5 | Customized surgical table, equipment and materials

To construct the spinal cord surgical station, two Thor labs 3-axis manipulators equipped with clamps were installed on an MB618 plate. In the middle of the clamps, two MB412 plates created slanted armrests for a customizable, 3D-printed surgical bed, following previous designs⁹. Additional components of gas delivery (Posi-vac, Patterson Scientific), active waste gas scavenging (EVAC 2, Patterson Scientific), vacuum aspirator (in-house vacuum flask), and isothermic bed (FHC) were integrated into the custom surgical set-up. For details see: (**Extended Data Fig. 1c**) and the GitHub containing CAD files of the individual 3D printed components.

Supplementary Note 6 | Machining and fabrication of the spinal chamber

We found that the magnetic attachment and covering the spinal window with tape to be a faster and more reliable cover method than attaching the cover with micro screws or using a sliding press fit around the side bars—due to the size, both methods increase the probability that the cover will snap or fall off. Note: to prevent accidental removal of the spinal chamber or animal distress due to immobility, it is critical when using the magnetic protective covers or mild steel stabilizing plate (as opposed to 316 stainless steel), to check that cages and all devices that animals interact with are non-magnetic.

The design modifications for the 3D printed (e.g. BioMed Clear) spinal chamber—side bars (1.0- and 2.0-mm thick) and stabilizing plates (1.5- and 2.0-mm thick)—improved the strength and reduced the probability that the pieces would snap during imaging. Furthermore, the stabilizing plate design includes chamfers on the side that adhere to the build plate. These chamfers make it easier to remove the pieces from the build plate with a chisel without damaging or snapping them. The side bars can be printed upside down and removed by chiseling under the tapered edge. We also tested and found that Surgical Guide (FormLabs) can substitute for BioMed Clear when 3D printing non-metallic pieces and is microCT compatible as well.

To create the side bars, we tested using CNC machining (Tormach, PCNC 1100). However, we found that this process introduced additional requirements, such as manufacturing additional jigs and devices to hold the side bars during tapering. Due to the small size of the side bars and the heat produced during the machining process, this often led to part failures or need for additional design and engineering to improve success rates. Further, this process is less accessible and more costly. It is also possible to have the pieces manufactured using commercial services entirely using CNC machining, which improves accessibility but is more costly per piece and introduces design limitations. These limitations are not present when laser cutting or 3D printing, including metallic 3D printing; we found these to be less expensive on a per-piece cost.

Supplementary Note 7 | Considerations and setups for *in vivo* spinal cord imaging

Spinal cord imaging requires fast acquisition due to the rapid and large shifts that can occur (**Extended Data Fig. 5h**). For example, we often conduct one-photon imaging with ≤ 10 ms exposure as longer exposures than that can lead to blurring (**Extended Data Fig. 7a**) and the scanning needed for two-photon imaging can lead to nonuniform distortions in the image⁵⁵. This need to anticipate large rostrocaudal spinal cord movements can also necessitate a large field of view (FOV) so as to ensure that biologically relevant features remain in the FOV regardless of spinal cord motion within (**Fig. 2c**) or across (**Fig. 3d**) sessions. One-photon imaging is generally preferred for fast and large FOV imaging due to availability of many commercial systems accessible to most labs. In addition, it is generally easier to give peripheral stimuli and monitor animals, as animals can be directly visualized whereas proper experimenter protection with two-photon imaging precludes certain types of experiments. However, due to optical limitations, imaging will be confined to superficial layers of the spinal cord⁵⁶ and resolution will oftentimes be worse compared to two-photon imaging. Reduced background fluorescence when imaging superficial neurons can be achieved using labeling approaches that predominantly label lamina I neurons but not lamina II (as is done here with SCPNs^{Phox2a}). Large FOV across multiple segments is commercially feasible with benchtop stereo and zoom microscopes (such as Zeiss Axio Zoom.V16 used in this study) assuming a high %QE, low read noise camera is used. We found a 2.3X objective with the Zeiss V16 allows us to image the entire FOV seen in most of our animals and also allows us to record real-color images of the spinal cord for later reference. Other methods, such as structured illumination^{57,58}, may allow further mitigation of background fluorescence. We discuss cameras, objectives, and photodamage considerations for one-photon imaging in greater detail in the following sections.

Deeper and higher-resolution imaging is possible with two-photon imaging, allowing monitoring of axons, cells, or similar structures. We recommend a 20x objective with at least 1.0NA, as it allows detection of individual cells and their processes (**Fig. 6c-d**). This leads to improved resolution and ultrasound gel or 3D printed wells can be used to mitigate evaporation of the immersion medium. Using a 20x/0.45NA objective did allow us to image individual nuclei in the spinal cord (**Fig. 3k**) and should thus be considered when aiming to avoid using a water objective or need the added working distance. However, if experiments necessitate the improved optical section from two-photon imaging while still desiring a large FOV, we found that the 5x/0.25NA objective can allow imaging of axons or other bright indicators (**Fig. 3g-h**). Care should be taken regarding field flatness of the objective, but this oftentimes is more critical when imaging slides and we found that the 5x/0.25NA objective works well in the spinal cord.

The main concern with two-photon imaging is that the smaller cross-section makes axial motion a larger concern, especially when combined with the large lateral movements. This limitation can be mitigated by fast volumetric scanning with deformable mirror, piezo objective scanners, or other approaches. Further, Bessel beams could further reduce sensitivity to axial motion by effectively imaging a volume but with additional spatial confinement and improve SNR offered by a Bessel focus⁵⁹. Recent work has demonstrated the ability to use adaptive optics or three-photon imaging to record from deeper layers of the spinal cord⁶⁰. Fortunately, adaptive optics are being integrated into commercial two-photon systems. Other approaches include using prisms³² or imaging the ventral horn using a modified surgical approach²⁴. As noted in the discussion, we anticipate newer techniques that allow large FOV and fast two-photon imaging to improve the depth, optical sectioning, and resolution afforded by multiphoton imaging, and which are applicable to the continued optical access provided by our method.

Lastly, when considering objectives or miniature microscopes, a working distance (WD) of at least 1.0 mm is recommended. In fact, a working distance of only ~ 300 μm , as is the case with some miniature microscope systems, will introduce challenges: once Teflon AF, Kwik-Sil, and coverglass are placed over the spinal cord, the distance from the top of the coverglass to the spinal cord can be >300 μm . Further, 1.0-mm WD gives an additional buffer in case there is cement or other material surrounding the coverglass. This could reduce how close the objective or baseplate (for miniature microscope mounting, see **Extended Data Fig. 9e-i**) can get to the coverglass and keep the tissue in focus.

Supplementary Note 8 | Optimizing *in vivo* spinal cord imaging: cameras and objectives

To collect imaging data amenable to high-quality downstream analysis, we needed to record videos with <10 ms exposure times that minimize the blurring that occurs during rapid and large shifts of the spinal cord (**Extended Data Fig. 7b**). For example, longer exposures would hinder accurate motion correction both within and across sessions, and limit quantitative measurement of fluorescence signals, especially when conducting Ca²⁺ imaging. And temporal downsampling of the movies to boost signal-to-noise (SNR) is not always viable as there can be significant motion (e.g. larger than the size of a cell) between individual frames (e.g. at normal 13-20 Hz acquisition with 10-ms exposure). However, this fast exposure time leads to issues with older CCD cameras that have high read noise, as that can diminish the signal-to-noise ratio (SNR) and the ability to detect biologically relevant signals, such as transients during Ca²⁺ imaging. Thus, we optimized several aspects of the preparation to maximize SNR and minimize blur. Modern sCMOS cameras greatly aided in achieving this aim. We tested several systems (see [One-photon imaging setup](#)) and found that those with quantum efficiency >90-95% in the 500-600 nm wavelength range and read noise <1.4 e⁻ RMS allowed for improved imaging quality compared to low quantum efficiency, high read noise CCDs or sCMOSes. For our initial studies, we collected data using a Photometrics CoolSNAP EZ CCD, then switched to the improved Photometrics Kinetix sCMOS, which boosted our SNR (as measured in Thy1-GFP slices and *in vivo* in the spinal cord) by an order of magnitude in certain cases. It is possible to use the effective global shutter in newer sCMOS cameras, such as the Kinetix, by only triggering the light source once all rows of the camera are acquiring data. This would further minimize the deformations seen due to fast rostrocaudal motion as the entire frame would be captured at once. This method contrasts with the majority of conventional fast-scanning (either with a galvo or resonant scanner) two-photon imaging systems, in which fast motion can often lead to deformations or missing data.

For bilateral spinal cord imaging of the entire or a large section of the FOV accessible post-laminectomy (**Fig. 4d**), we optimized imaging conditions by combining low-magnification objectives (4X/0.16NA, 5x/0.16NA, or 5x/0.25NA) with large-sensor sCMOS cameras (e.g. Photometrics Kinetix). Further, we wanted to minimize the effects of axial (dorsal-ventral) motion, which would cause cells to drop out or lead to significant changes in fluorescence intensity not related to Ca²⁺ activity. Another advantage of one-photon imaging with low-magnification objectives is the larger depth-of-field, which reduces sensitivity to dorsal-ventral (axial) motion. This feature reduces the need to compensate for axial motion with fast volumetric acquisition. Because the low-magnification objectives often have a lower NA, we tested a series of objectives and found that the Zeiss Fluor 5x/0.25NA objective, both theoretically and when measured, obtained the highest signal while having a tolerable field flatness that still allowed bilateral imaging of dorsal horn lamina I neurons and glia.

Supplementary Note 9 | Optimizing *in vivo* spinal cord imaging: reducing photodamage

Below we discuss a subset of strategies that can be used to reduce photodamage and thus improve long-term imaging. A number of methods exist to reduce phototoxicity and photobleaching while improving signal, such as pulsed illumination, co-illumination by main excitation and secondary light source to reduce bleaching, and selected illumination (illuminating only biologically relevant areas). These methods take advantage of bio- or photophysical properties of fluorescent molecules.

Pulsed illumination aims to reduce the percent of bleached molecules by illuminating in short microsecond or millisecond pulses. Photons excite fluorescent molecules from S_0 to S_1 singlet state, wherein it can either (1) release a photon (after several nanoseconds) and return to S_0 , (2) become excited to further singlet states ($S_{n>1}$), and (3) become bleached, or undergo intersystem crossing (ISC) to a triplet state (T_1). In this triplet state, the fluorophore can be further excited to higher triplet states and also become bleached. While relaxation to lower triplet states can take picoseconds, relaxation from the lowest triplet state (T_1) to the lowest singlet state (S_0) can take microseconds. Thus, by pulsing the illumination with microsecond spaced gaps, this allows additional time for fluorophores in the triplet state to return to the singlet state rather than being pushed to higher triplet states or becoming bleached. In theory it would also improve signal with less light input as a smaller number of fluorophores would be bleached⁶¹. Experimentally, pulsed illumination previously led to improved signal at equivalent pulse intensities *in vitro*⁶², reduced *C. elegans* photobleaching⁶³, and reduced photobleaching in cell or primary cultures^{64–66}. Further, pulsed illumination may allow heat dissipation or reactive oxygen species scavenging between illumination periods, further reducing potential tissue damage. It is critical to note that the photophysics time constants can vary by an order of magnitude depending on the fluorophore⁶⁷, which will determine the timescale of pulsed illumination and potential benefits seen.

Another strategy would be to induce fluorescent proteins into states that more rapidly convert from triplet to singlet states. A recent report suggests that using near-infrared can excite EGFP to higher triplet states, which leads to reverse intersystem crossing (RISC) and thus is protective against bleaching⁶⁸. This report demonstrated that this reduces photobleaching 1.5–9.2-fold in cell culture and we anticipate that this strategy may prove useful in certain instances *in vivo*.

Illuminating only biologically relevant areas reduces the overall phototoxicity but requires pre-knowledge about biologically interesting areas. Controlled light-exposure microscopy (CLEM) is one method⁶⁹ and a number of groups have used similar concepts, such as using random access scanning for fast two-photon imaging of samples while reducing photodamage to a given cell⁷⁰. However, in the spinal cord, these techniques will need to be adapted to handle the potentially large and rapid rostrocaudal motion (**Extended Data Fig. 5h-i**). This might be possible using fast real-time tracking of motion to compensate⁷¹. These techniques can each be considered and tested experimentally for users conducting spinal cord imaging; however, we demonstrate hours-long imaging with our existing one-photon imaging (**Fig. 4m** and **Extended Data Fig. 9q**). Thus, we recommend attempting imaging without these optimizations and only using them if experimental artifacts are observed.

Supplementary Note 10 | Processing, display, and 3D rendering of microCT data

For the model used to display the spinal cord implant chamber in **Fig. 1a**, we performed a virtual laminectomy by manually removing the overlying spinous process and lamina. Then to create a smooth surface mesh, we eliminated non-manifold edges and closed holes created by face removal. We exported the final mesh from MeshLabs as an STL file. We then imported files into FreeCAD for conversion from a mesh to a solid by converting the mesh to a shape and then converted the shape to a solid before exporting as a STEP file. To visualize 3D renders, we imported the resulting STL (MeshLabs) or STEP (FreeCAD) files into PTC Creo 6.x or 9.x. We converted spatial units to mm and scaled the model 1000:1 to match the size and coordinate system commonly used in the rodent by checking that bregma to lambda distance was ~4.2-mm, as expected. To display high-quality photorealistic renders, we assigned components realistic textures (e.g. metal, glass, etc.) along with using bump maps to simulate rough surfaces. These bump maps are not used when 3D printing or otherwise manufacturing the components and are purely for visual aid to the readers. We then used the Renderer module within PTC Creo with 64 direct bounces, 64 indirect bounces, quality level 5 shadows, and enabled global illumination, caustics, and interior lighting. For surgery videos, we used the Animation module within PTC Creo and a series of views and snapshots of the spinal implant components in various configurations. To minimize noise on each frame, we ran 2 min of rendering time per frame (~4000–4500 samples) on a NVIDIA A5000 GPU. We saved the animation as an uncompressed AVI, which was then converted to an mp4 with ffmpeg before use in the surgery videos (**Supplementary Video 2-4**).

Supplementary Note 11 | Additional details of the rotarod assay

As the rotarod assay is a test of motor learning as well as motor coordination, we also evaluated and recorded animals for 3 trials during a single behavior session (one session per day). For each trial, we placed animals on the rod and positioned them facing in the direction opposing the rod's motion, which minimized the chance that they would immediately fall off when facing the direction of motion. The rod started at 4 rotations/min and increased at a consistent rate to 30 rotations/min for 5 mins. The final speed was maintained until the animal fell off. Animals had at least 3 mins between trials within a single day's session; if we ran more than five animals during a single session, the time between sessions was at minimum the time taken to run all other cohorts of mice. Animals can "flatten" themselves onto the rotarod and thus hang onto the rod after they would have been evaluated as failing the task. This can lead to incorrect automatic measurement of the latency to fail the task and introduces different metrics between animals that fall and those that can wrap their bodies around the rotarod, which can also differ by age and body size. To circumvent this, we used cameras (The Imaging Source, DMK 21AU04 and DFK 42BUC03) to record all rotarod sessions and post-hoc determined the time when the animals either fell or hung into the rod and began their first circle around the rotarod.

Supplementary Note 12 | Body part annotation during behavior video analysis

We chose to track several body parts based on their high probability of being in the camera FOV in almost all frames in an imaging session and likelihood of exhibiting motion during nocifensive behavior. We manually annotated the nose, eyes, tip and base of the ears, forepaws, hindpaws, and base of the tail. We separately annotated left and right hind and forepaws across the left and right facing cameras, respectively. In the bottom facing camera we annotated all body parts. For the purposes of downstream analysis, owing to the rigid nature of the face, we did not distinguish between left or right sides of the eyes, ears, or mouth and combined the analysis of multiple views of each regardless of the side of the body. We combined the tracking of the ear tip and base to simplify analysis. For some videos, such as in **Fig. 4g**, we annotated a fixed bar to create a stationary control object to demonstrate stability of recording and tracking along with specificity of animal movement. It is possible to calibrate multiple cameras to enable 3D tracking of animal body parts⁷². This enables more detailed analysis of body part movements, but increases the complexity of the setup and requires additional calibration steps.

Supplementary Note 13 | Feature selection for accurate LD-MCM motion correction

We used several criteria to select features for LD-MCM. Animals with prominent dorsal veins and dorsal ascending venules (dAV) made possible the most robust motion correction owing to the existence of distinct, stable landmarks. We selected features based on a series of criteria: feature is stable within individual and across most of the imaging sessions of an animal as determined visually (by rapid scrolling through the field of view); feature is “distinct”, e.g. a blood vessel with a branch is easier to consistently annotate the correct position compared to an unbranched vessel; and the feature’s motion is concordant with the motion of the biological features of interest, e.g. spinal cord vasculature motion matches those of dorsal horn neurons or microglia. Note that features that disappear from the FOV (see **Supplementary Video 10**) can still be annotated, but depending on the motion correction transformation type used, we discard them from specific frames and only use commonly found, high-confidence features between the reference and the to-be-corrected frame.

There are some features that on particular sessions have deviated enough from the training dataset and thus resulted in inconsistent labeling. This can be due to a change in the vasculature size, e.g. if a vessel diameter becomes smaller during different arousal states (compared to the sessions used to train the model) or when the vessel disappears during the course of long-term imaging. These features can hamper motion correction and thus should be removed. As large movement of the FOV often is correlated across all feature points (**Extended Data Fig. 5h**), it is possible to calculate the per-frame displacement correlation coefficient between all features and eliminate those that fall outside a predefined range (**Extended Data Fig. 5d**). We did this via manual inspection, but clustering or using a cut-off criterion of the mean correlation of each feature to all other features can also be used.

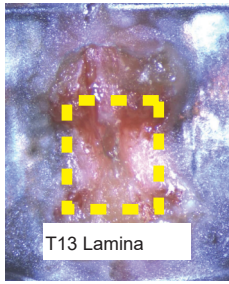
Supplementary Note 14 | Cross-session fluorescence intensity normalization methods

We used the following method to compensate for changes in fluorescence intensity values across multiple CCD and sCMOS cameras used in the study during one-photon imaging. For the first, we imaged GFP+ cells in the same area of the basolateral amygdala, from a slide containing 100- μ m thick sections from a Thy1-GFP-M mouse. This was repeated with each camera using the same objectives used for each animal (e.g. Fluar 5x/0.25NA). To only include GFP+ signal in the calculation, we identified cells and extracted their mean signal intensity using a custom MATLAB function in which we identified cells by applying the following operations: spatial bandpass filtering (keep spatial frequencies 5-40 cycles), detected edges using the Sobel method, dilated the edges and filled the holes to identify cell shapes, removed any cells at the border of the image, eroded the binary image to further separate cells and eliminate noise, and then segmented cells (using *regionprops* in MATLAB). We calculated the mean signal based on all pixel values inside each segmented cell's binary mask. To produce the cross-session fluorescence intensity curves, we then constructed a correction factor for each camera relative to the mean signal from the CoolSNAP EZ camera and divided the total whole-frame fluorescence intensity values by this correction factor. This procedure corrected for the large disparity in intensity values, but still produced residual differences, likely owing to differences between GCaMP and GFP expression across animals and to slight changes in the imaging setup when cameras were swapped or during routine maintenance.

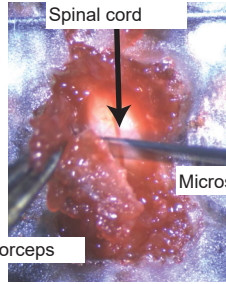
SUPPLEMENTARY FIGURES

 <p>Side post</p>	<p>Position the animal so that the lumbar enlargement (hump of the back) is in line with the side posts. (Step 1.)</p>	 <p>Kwik-Sil</p>	<p>Apply Kwik-sil to protect the intervertebral tissue. (Step 11.)</p>
 <p>T13</p>	<p>Open ~1 cm of skin along the midline. Identify the T13 vertebra. (Steps 2-3.)</p>	 <p>Superglue</p>	<p>Apply Superglue drops to connect the needles and Side Bars. (Step 12.)</p>
 <p>Lamina</p> <p>Intact paraspinous muscle</p> <p>T12</p> <p>T13</p> <p>L1</p>	<p>Microdissect paraspinous muscle to expose the T12-L1 laminae. Preserve intervertebral tissue. (Steps 4-7.)</p>	 <p>Suture</p>	<p>Close skin around the Side Bars with a suture and VetBond. (Steps 13-14.)</p>
 <p>Left Lamina</p> <p>Right Lamina</p> <p>Intervertebral space covered with Surgifoam</p>		 <p>Superglue</p>	<p>Release side post clamps. Add Superglue to each Side Bar handle. (Steps 15-16.)</p>
 <p>T12 DSP</p>	<p>Insert a 33G needle through the T12 dorsal spinous process (DSP) and snip. (Step 8.)</p>	 <p>Stabilizing plate</p>	<p>Manually place the Stabilizing plate over the Side Bar handles and squeeze together to glue. (Step 16.)</p>
 <p>L1 DSP</p>	<p>Repeat needle insertion through the L1 DSP and snip. (Step 8.)</p>	 <p>Superglue</p>	<p>Clamp the Stabilizing plate and Side Bars together with the side posts and apply more Superglue. (Step 17.)</p>
 <p>Side Bars</p>	<p>Clamp the Side bars to the side posts. Lift the needles until they sit over top of the Side Bars. (Step 9.)</p>	 <p>Cement</p>	<p>Prepare the surface of the laminae by scraping. Recommended: use dentin activator. (Steps 17-18.)</p>
 <p>Side Bars</p>	<p>Advance the Side Bars towards the vertebrae. Tuck skin underneath the Side Bars while advancing. (Step 10.)</p>	 <p>Cement</p>	<p>Apply cement over the field except the T13 lamina. (Step 19.)</p>
 <p>Side Bars</p>	<p>Adjust the Side Bars lower and level with each other. Press down on T13. Advance the Side Bars to their final position against the vertebrae. (Step 10.)</p>	 <p>T13</p>	<p>Confirm access to T13 lamina before the cement sets. (Step 20.)</p>
 <p>Side Bars</p>	<p>Adjust the Side Bars lower and level with each other. Press down on T13. Advance the Side Bars to their final position against the vertebrae. (Step 10.)</p>	 <p>Kwik-Sil</p>	<p>Coat T13 lamina with Kwik-Sil for protection until laminectomy. (Step 21.)</p>

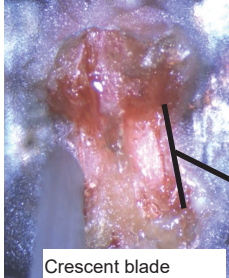
Supplementary Fig. 1 | Key frames of the first procedure - Chamber implantation
 Three metal pieces are implanted paraspinally, in 21 steps.



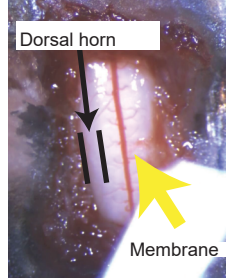
Remove Kwik-Sil. Reduce cement at the edges of the T13 lamina with a microdrill. (Step 1.)



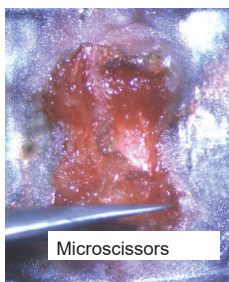
Raise lamina from underneath with a dull spatula and remove. (Steps 3-4.)



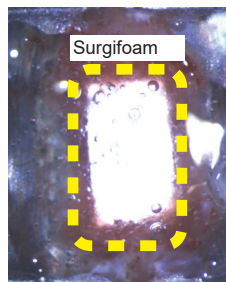
Cut through the lamina on each side. (Step 2.)



Separate dura and cut the PRECLUDE membrane to fit the laminectomized area, and then place membrane. (Steps 5-7.)

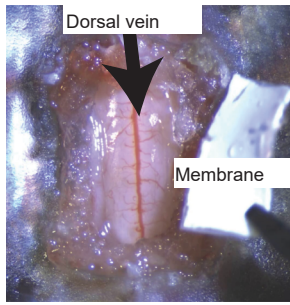


Cut through the intervertebral tissue. (Step 3.)

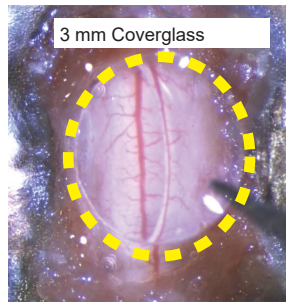


Surround the PRECLUDE membrane with Surgifoam, and then coat with Kwik-Sil. (Steps 8-9.)

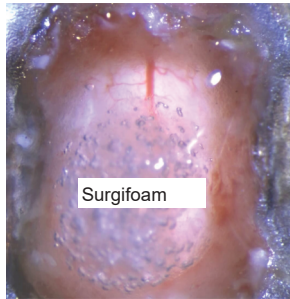
Supplementary Fig. 2 | Key frames of the second procedure - Laminectomy
 1 week or more after the bar-implantation, a laminectomy is performed in 9 steps.



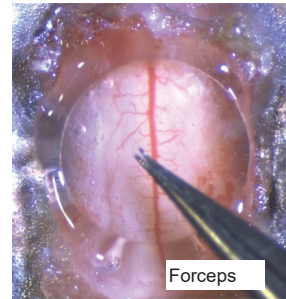
Remove Kwik-sil & membrane. The spinal cord will be visible. (Step 1.)



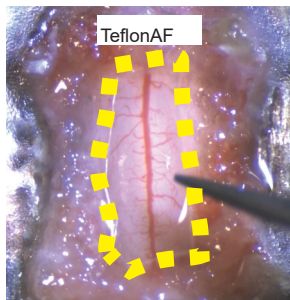
Immediately place a 3 mm coverglass over the Kwik-sil. (Step 5.)



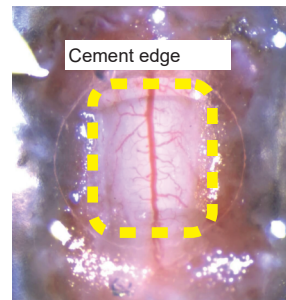
Cover the spinal cord with wet Surgifoam. (Step 2.)



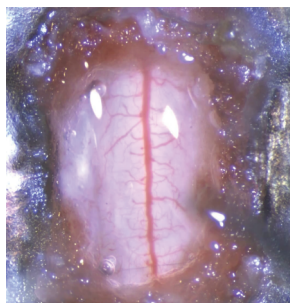
Press down on coverglass. Allow Kwik-Sil to harden for 10 minutes (Step 5-6.)



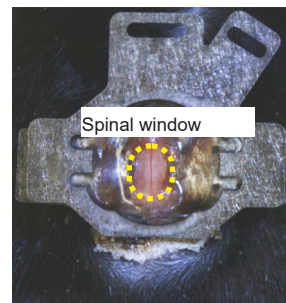
Shape a piece of TeflonAF to the size of the exposed spinal cord. Place directly onto the cord. (Step 3.)



Seal the edges of the glass with cement or optical adhesive. (Steps 7.)

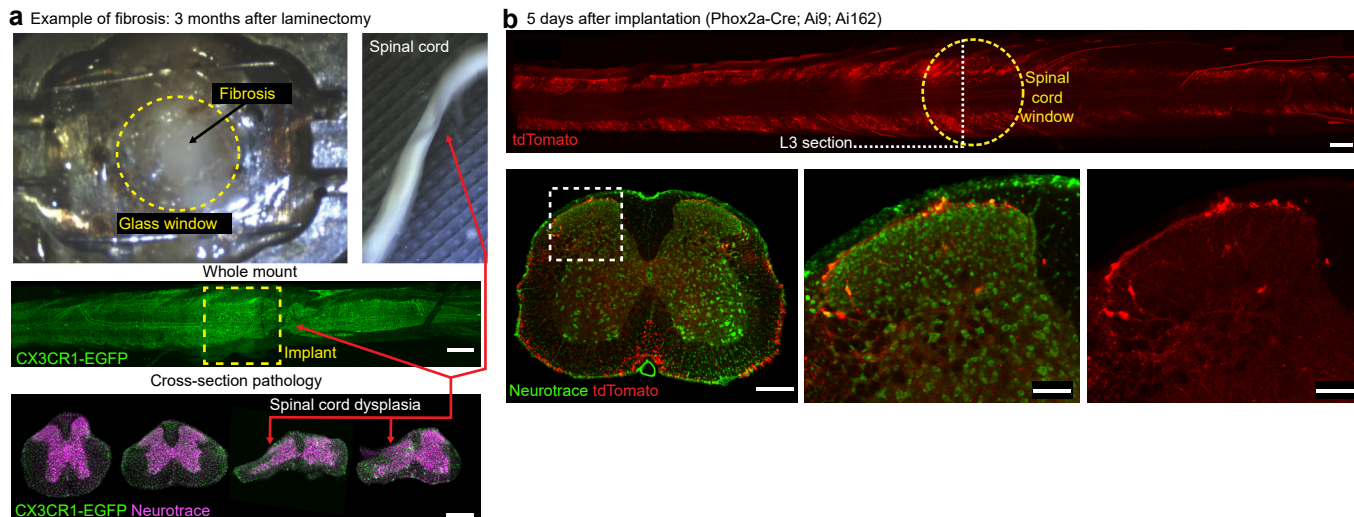


Apply a drop of Kwik-Sil over the TeflonAF. (Step 4.)



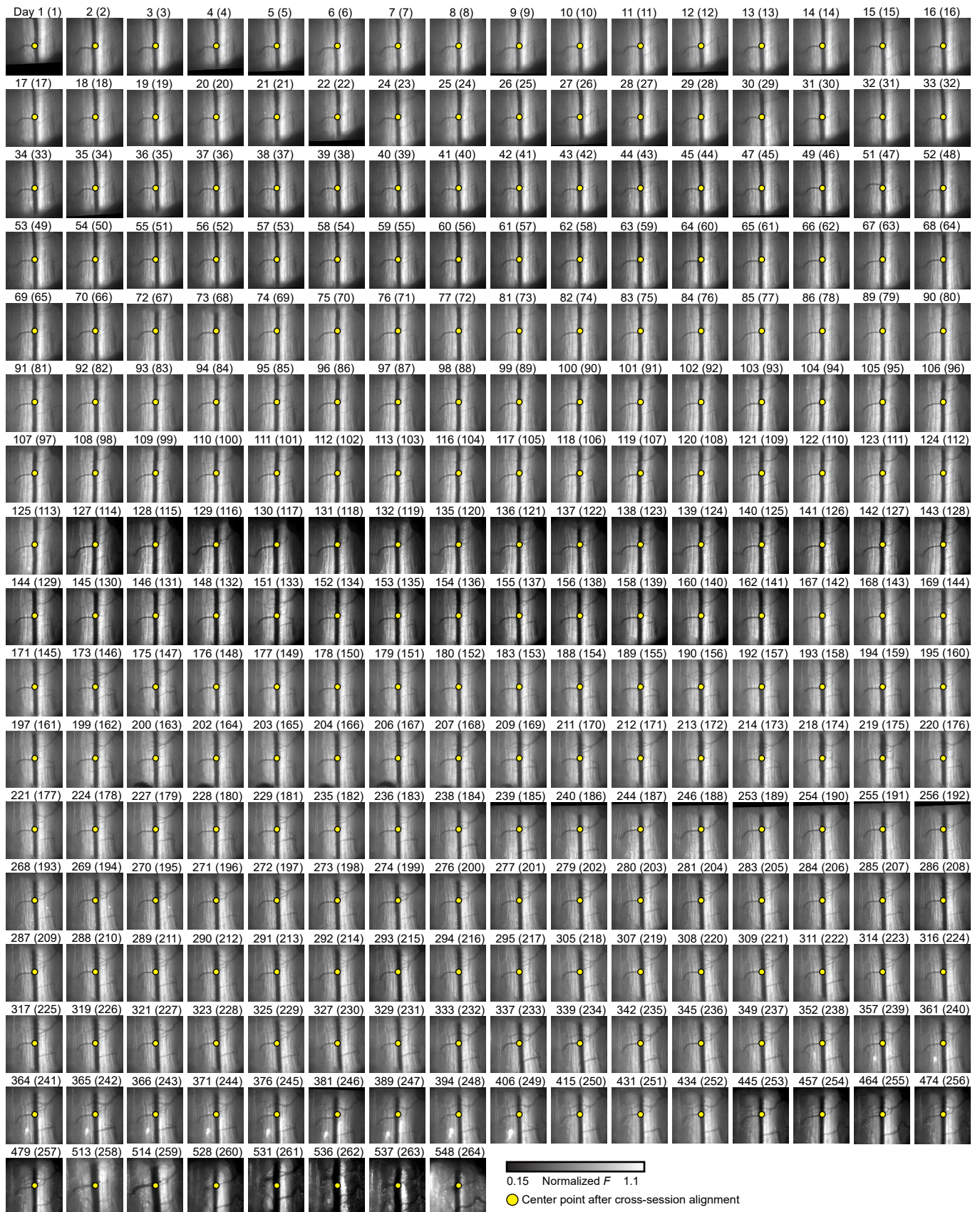
Window is sealed and ready for imaging.

Supplementary Fig. 3 | Key frames of the third procedure - Spinal cord window placement
A glass window is installed in 7 steps.



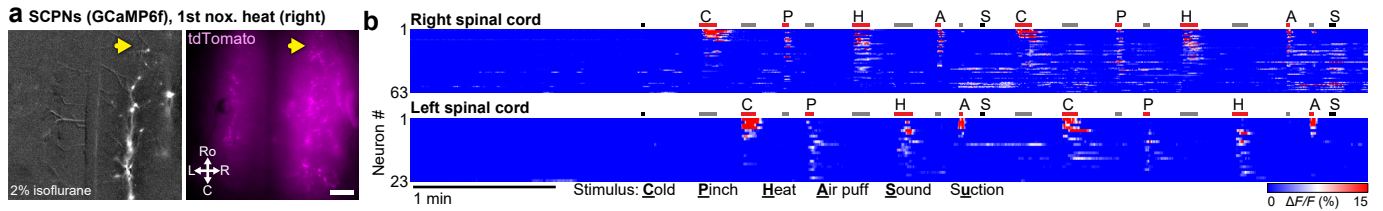
Supplementary Fig. 4 | Histological analysis post chamber implant and laminectomy

a, Post-mortem examination of a mouse that developed fibrosis after 3 months of imaging. Fibrosis is associated with a whitish spongy tissue filling the space beneath the coverslip and displacing the spinal cord. Scale bars, 1 mm (whole-mount) and 500 μ m (coronal slices). **b**, Spinal cord histology of a Phox2a-Cre; Ai162; Ai9 (LSL-tdTomato) mouse 5 days after chamber implant. Superficial lamina I projection neurons (tdTomato, red) are visualized by whole-mount and a cross-section of L3 with a Neurotrace (green) counter-stain. tdTomato+ neurons are found in their appropriate laminae 1 and 5 locations. The dashed yellow circle shows the target location for the spinal cord window. Scale bars, 500 (whole-mount), 300 (coronal slice), and 100 μ m (zoomed coronal slices). **a**, **b** are representative sections from a single experiment.



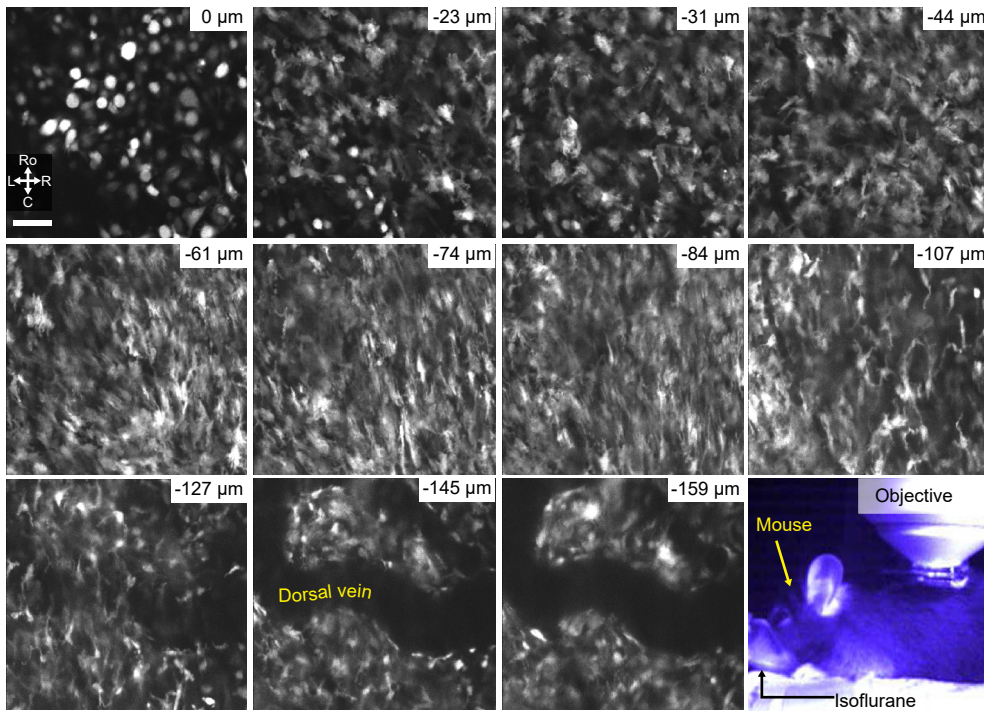
Supplementary Fig. 5 | Long-term imaging of axons in the spinal cord of awake mice

Individual frames from 264 imaging sessions from the spinal cord of a Thy1-GFP mouse imaged for 548 days after cross-session alignment with CS-MCM. Red dot indicates the center of the field of view, near the intersection of the dorsal vein and a dorsal ascending venule. For display purposes, because different cameras were used during certain imaging sessions, here each frame is displayed between the 0.1th to 99.5th percentile of movie pixel values. See video at Supplementary Video 10. Numbers in parentheses are session numbers. Scale bar, 200 μm .



Supplementary Fig. 6 | Imaging of spinal cord neuronal activity in anesthetized animals

a, $\Delta F/F$ processed GCaMP and raw tdTomato frames from Phox2a-Cre; Ai148 (GCaMP6f); Ai9 (tdTomato) mouse under general anesthesia (2% isoflurane) shows overlap in expression. Yellow arrow: side on which stimulus was presented. Scale bar, 300 μm . **b**, Activity of individual SCPNs (GCaMP $\Delta F/F$) on the left and right spinal cord during a single imaging session (5.15 min, 20 Hz) during application of various noxious and non-noxious stimuli. There is a ~ 2 min baseline period at the start of the session, prior to stimulus presentation.



Supplementary Fig. 7 | Multiplane two-photon imaging of CX3CR1-EGFP mouse

Multi-plane, two-photon imaging of monocytes (meninges) and microglia (spinal cord) in an anesthetized mouse (2% isoflurane) from the meninges (top-left) into the spinal cord (bottom-right, beginning at -127 μm). Each image is the mean image of 10 time points (~ 50 s, 0.2 Hz). Depth is relative to meninges. Scale bar, 50 μm . See video at Supplementary Video 16.

SUPPLEMENTARY TABLES

Supplementary Table 1 | Chamber implant step-by-step

The following step-by-step surgical procedures are complemented by diagrams in **Supplementary Fig. 1** and **Supplementary Videos 2**.

Step	Description of surgical steps (chamber implant)
-	Pre-op checklist: Sterilize tools, sterilize implantable components (side bars & stabilizing plate), wet hemostatic sponge (Surgifoam) with saline, prepare 0.5% lidocaine solution, weigh mouse and prepare NSAID analgesic, induce anesthesia, stabilize body temperature and respiratory rate, apply eye ointment, remove hair over the lumbar enlargement, disinfect the skin, administer NSAID analgesic.
1	Position the animal on the surgical table so that the lumbar enlargement is in line with the side posts. <i>Note:</i> Drape the surgical field to improve sterile technique.
2	Confirm loss of the toe pinch reflex, then incise and open ~1.0 cm of skin along the midline overlying the lumbar enlargement. <i>Note:</i> Apply intra-incisional lidocaine.
3	Locate the T12, T13, and L1 vertebrae.
4	Using sharp, pointed microscissors, penetrate fascia and paraspinal muscles lateral to each dorsal spinous process (DSP) of T12, T13, and L1 vertebrae, and elevate muscles from laminae by blunt dissection. <i>Note:</i> Apply Surgifoam if there is bleeding.
5	Lift and cut away the loose paraspinal muscle lateral to the T12, T13, and L1 DSPs. <i>Note:</i> Do not cut into the intervertebral muscle. <i>Note:</i> To maintain tissue hydration until Step 11, place saline-soaked Surgifoam over the intervertebral muscle.
6	Sever the thick tendons connected to the articular processes of T13. <i>Note:</i> To more easily reveal these tendons, open a retractor under the muscles overlying the T13 lamina.
7	Wipe or scrape clean the bone surfaces of all laminae & DSPs. <i>Note:</i> If necessary, remove any remaining muscle adhered to the laminae.
8	Insert a 33G needle through the T12 DSP and snip the base of the needle. Repeat at L1 DSP.
9	Clamp the side bars to the side posts and slide each into the surgical field. Lift the needles until they sit over the top of the side bars.
10	Use a micro spatula to progressively tuck the exposed muscle and skin slowly under the side bars while advancing the side bars towards and against the vertebral column. <i>Note:</i> Adjust the vertebral column by pressing down on T13 and lowering the side bars before the side bars contact the vertebrae. <i>Note:</i> To create a flat base for stabilizing plate attachment (Step 16), level the side bars with each other.
11	Remove all saline-soaked sponges, blot the field dry, and immediately make a discrete Kwik-Sil mask to cover all intervertebral spaces.
12	Affix needles to the side bars with Superglue contacts.
13	As the glue dries, suture the incised skin together rostral and caudal to the side bars.
14	Adjacent to the suture, seal the rostral and caudal tissue border with a moderate amount of Vetbond.
15	To free the side bar and needle construction, release the side post clamps.
16	Apply Superglue onto each side bar handle and then place the stabilizing plate over top and manually squeeze so as to glue together and then re-engage the side clamps. <i>Note:</i> Add additional Superglue at the inside notches of the stabilizing plate when clamped.

Step	Description of surgical steps (chamber implant)
17	To maximize the area of bone cement binding, scrape the exposed laminar bone of each vertebra, without disrupting the intervertebral mask.
18	To further prepare the bone for bone cement binding, apply dentin activator gel to bone surfaces for 15 seconds; then rinse off with saline and blot dry.
19	Generously apply free-flowing cement to the field, coating the prepared bone, DSP needles, and side bar edges.
20	To access the T13 lamina for future laminectomy, immediately clear any cement from the T13 lamina before it sets.
21	Finally, to protect the exposed lamina until laminectomy, coat the T13 lamina and surrounding cement with Kwik-Sil.
-	Post-op checklist: Provide heat, monitor recovery, and administer opioid analgesic.

Supplementary Table 2 | Laminectomy step-by-step

The following step-by-step surgical procedures are complemented by diagrams in **Supplementary Fig. 2** and **Supplementary Videos 3**.

Step	Description of surgical steps (laminectomy)
-	Pre-op checklist: Weigh the mouse and prepare NSAID analgesic, induce anesthesia, stabilize body temperature and respiratory rate, and apply eye ointment.
1	Remove the Kwik-Sil coat over the T13 lamina. <i>Note:</i> If necessary, reduce cement at the edges of the T13 lamina with a microdrill burr.
2	Cut through the lamina as laterally as possible, on both sides.
3	Transect the intervertebral ligaments to free the lamina and then remove the lamina <i>Note:</i> Take care to separate any attachments to the lamina before pulling away.
4	Immediately add saline-soaked hemostatic sponge over the spinal cord to maintain hydration and stop any bleeding.
5	Incise the dural layer and retract laterally to expose the spinal cord and replace the hemostatic sponge. <i>Note:</i> widen the laminectomy, if necessary, to expose the characteristic grayish hue of the dorsal horn.
6	Shape a single piece of the PRECLUDE membrane to the size of the exposed spinal cord.
7	Remove Surgifoam and place the PRECLUDE membrane directly over the spinal cord.
8	Place a small amount of saline-soaked Surgifoam around the border of the Preclude membrane (this helps limit ingrowth).
9	Blot dry the Surgifoam and apply Kwik-Sil to close off the entire field and hold the Preclude membrane in place until window placement.
-	Post-op checklist: Provide heat, monitor recovery, and administer NSAID analgesics.

Supplementary Table 3 | Window placement step-by-step

The following step-by-step surgical procedures are complemented by diagrams in **Supplementary Fig. 3** and **Supplementary Videos 4**.

Step	Description of surgical steps (window placement)
-	Pre-op checklist: Weigh the mouse and prepare NSAID analgesic, induce anesthesia, stabilize body temperature and respiratory rate, and apply eye ointment.
1	Remove the Kwik-Sil coat and PRECLUDE membrane to expose the spinal cord.
2	Immediately add saline-soaked hemostatic sponge over the spinal cord to maintain hydration and stop any bleeding. Note: If necessary, any remaining surgifoam that surrounded the PRECLUDE in the previous operation may be removed to expand the exposed area of the spinal cord.
3	Shape a single piece of the Teflon AF membrane to the size of the exposed spinal cord. Remove the hemostatic sponge and quickly blot the field dry with a cellulose sponge. Immediately place the shaped Teflon AF membrane directly over the spinal cord.
4	Add a small amount of Kwik-Sil to flow over the Teflon AF & laminectomy area.
5	Immediately set a 3.0-mm circular coverslip. Note: Press down on the coverslip for 1 second to squeeze out the excess Kwik-Sil adhesive; this may be repeated twice.
6	Allow Kwik-Sil adhesive to harden untouched for 10 min.
7	Permanently set the coverslip with bone cement or Norland optical adhesive Note: Completely cover the edges of the Kwik-Sil layer to seal the preparation.
-	Post-op checklist: Provide heat, monitor recovery, and administer NSAID analgesics.

Supplementary Table 4 | Materials used for *in vivo* imaging of the mouse spinal cord

Item	Vendor	Product No.	Website	Experiment/Note
Analgesics				
Ethiqa XR	Fidelis Animal Health, Inc.	86084-100-30	https://ethiqaxr.com/	Surgery (general use)
Lidocaine	Hospira Inc	0409-2066-10	https://www.pfizermedicalinformation.com/en-us/lidocaine/principal-display	Surgery (general use)
Carprofen	Zoetis Inc.	54771-8507-01	https://www.pattersonvet.com/ProductItem/078447425#productSpecificationsTab	Surgery (general use)
Buprenorphine	PAR Pharmaceutical	42023-179-05	https://www.parpharm.com/products/sterile/buprenorphine-hcl-injection/	Surgery (general use)
Proparacaine HCL Ophthalmic	Medline Industries	24208-730-06	https://www.medline.com/product/Proparacaine-HCL-Ophthalmic/Ophthalmic-Medications/Z05-PF87216?qu_4	Topical eye analgesic (retro-orbital injections)
Implantable components				
304 stainless steel	McMaster Carr	8983K114, 8983K113, 8983K111, 3254K322	* https://www.mcmaster.com/products/304-stainless-steel/multipurpose-304-stainless-steel-6/ * https://www.mcmaster.com/3254k322/	Implant
316 stainless steel	Proto Labs	316L CL 20ES	https://www.protolabs.com/services/3d-printing/direct-metal-laser-sintering/stainless-steel/	Implant
Laser-cutting service	Laser Alliance LLC	Milpitas, CA	https://laseralliance.com/	Implant
BioMed Clear	Form Labs	RS-F2-BMCL-01	https://formlabs.com/store/materials/biomed-clear-resin/	Implant
Surgical Guide	Form Labs	RS-F2-SGAM-01	https://formlabs.com/store/materials/surgical-guide-resin/	Implant
Grinding Wheel	WEN	4276 2.1-Amp 6-Inch	https://wenproducts.com/products/wen-bg4276-2-1-amp-6-inch-single-speed-bench-grinder-with-flexible-work-light	Implant
3D printed covers	Stratasys	uPrint ABS		Implant Cover
3D printed covers	Makerbot	Nylon 12 Carbon Fiber [375-0061A] or ABS-R [375-0071A]		Implant cover
Neodymium magnets	MacMaster Carr	5862K141	https://www.mcmaster.com/5862K141/	Implant Cover
Light Cure Adhesive LOCTITE 4311	Henkel	HL1401789	https://www.henkel-adhesives.com/us/en/product/uv-curing-adhesives/loctite_43110.html	Implant Cover
Surgery Station Equipment				
Compact Flexure Plate Clamp, 1/4"-20 Tap	Thorlabs	PC2	https://www.thorlabs.com/thorproduct.cfm?partnumber=PC2#ad-image-0	Clamps (surgery station)
Ø1/2" Optical Post, 1/4"-20 Tap, L = 6"	Thorlabs	TR6	https://www.thorlabs.com/thorproduct.cfm?partnumber=TR6	Posts (surgery station)
RA90 - Right-Angle Clamp for Ø1/2" Posts, 3/16" Hex	Thorlabs	RA90	https://www.thorlabs.com/thorproduct.cfm?partnumber=RA90	Posts (surgery station)
1/2" XYZ Translation Stage with Standard Micrometers, 1/4"-20 Taps	Thorlabs	PT3	https://www.thorlabs.com/thorproduct.cfm?partnumber=PT3#ad-image-0	XYZ micromanipulators (surgery station)
Aluminum Breadboard, 6" x 18" x 1/2", 1/4"-20 Taps	Thorlabs	MB618	https://www.thorlabs.com/thorproduct.cfm?partnumber=MB618	Base (surgery station)
Aluminum Breadboard, 4" x 12" x 1/2", 1/4"-20 Taps	Thorlabs	MB412	https://www.thorlabs.com/thorproduct.cfm?partnumber=MB412	Arm rests (surgery station)
Surgical Table (60" x 30")	McMaster-Carr		* https://www.mcmaster.com/4380T12/ * https://www.hubert.com/product/PJB.ST6-3060SBK/John-Boos-16GA-60X30-FLAT-WADJ-SS-BRC-KD	Surgery station
Homeothermic system	FHC	40-90-8D; 40-90-5D-02;	https://stoeltingco.com/Neuroscience/Homeothermic-Blanket-System-9905	Heating system (Surgery Station and acute imaging)
RightTemp® Jr. Heating Pad	Kent Scientific	RT-JR-15	https://www.kentscientific.com/products/righttemp-jr/	Surgery (general use)
Posi-Vac nosecone	Patterson Scientific	78914730	https://www.pattersonscientific.com/posi-vac-nonrebreathing-system/	Surgery (general use)
Isoflurane vaporizer system	VetEquip	911103	http://www.vetequip.com/item.asp?cat=3&catalogID=911103-6	Surgery (general use) and acute imaging)

Item	Vendor	Product No.	Website	Experiment/Note
EVAC 2 Waste Anesthetic Gas Evacuation System	Patterson Scientific	078918181 (Charcoal filter 78909457)	https://www.pattersonscientific.com/evac-2-evacuation-vacuum-attenuation/	Surgery (general use and acute imaging)
Pump 11 Elite Nanomite Infusion/Withdrawal Programmable Syringe Pump	Harvard Apparatus	70-4507	https://www.harvardapparatus.com/re mote-infuse-withdraw-pump-11-elite-nanomite-programmable-syringe-pump.html	Surgery (intrasplinal injections)
Camera	The Imaging Source	DFK 33UX183c, IC Capture 2.5	https://www.theimagingsource.com/en-us/product/industrial/33u/dfk33ux183/	Window optical clarity validation
3D printed nose cone holder	Custom			Surgery (general use)
3D printed mouse surgery table/platform	Custom	Modified design from ⁹ .		Surgery (general use)
Surgical reagents & tools				
SURGIFOAM® Absorbable Gelatin Sponge	Ethicon	1972	https://www.ethicon.com/na/epc/code/1972	•Surgery (general use, hemostatic) •Similar to Gelfoam
Micro-Adson Forceps	Fine Science Tools	11018-12	https://www.finescience.com/en-US/Products/Forceps-Hemostats/Standard-Forceps/Micro-Adson-Forceps/11018-12	Surgery (general use)
Graefe Forceps	Fine Science Tools	11051-10	https://www.finescience.com/en-US/Products/Forceps-Hemostats/Standard-Forceps/Graefe-Forceps/11051-10	Surgery (general use)
Dumont #2 - Laminectomy Forceps	Fine Science Tools	11223-20	https://www.finescience.com/en-US/Products/Forceps-Hemostats/Dumont-Forceps/Dumont-2-Laminectomy-Forceps/11223-20	Surgery (general use)
Dumont #5 - Fine Forceps	Fine Science Tools	11254-20	https://www.finescience.com/en-US/Products/Forceps-Hemostats/Dumont-Forceps/Dumont-5-Fine-Forceps/11254-20	Laminectomy
Dumont #3c Forceps	Fine Science Tools	11231-20	https://www.finescience.com/en-US/Products/Forceps-Hemostats/Dumont-Forceps/Dumont-3c-Forceps/11231-20	Spared nerve injury
Fine Scissors - Sharp	Fine Science Tools	14060-10	https://www.finescience.com/en-US/Products/Scissors/Standard-Scissors/Fine-Scissors-Sharp/14060-10	Implant
Spring Scissors - 8mm Cutting Edge	Fine Science Tools	15023-10	https://www.finescience.com/en-US/Products/Scissors/Spring-Scissors/Spring-Scissors-(1)/15023-10-(1)	Implant
Spring Scissors - Angled	Fine Science Tools	15010-09	https://www.finescience.com/en-US/Products/Scissors/Spring-Scissors/Spring-Scissors-Angled/Spring-Scissor-Angled-2mm	Laminectomy
Tissue Separating Scissors	Fine Science Tools	14072-10	https://www.finescience.com/en-US/Products/Scissors/Standard-Scissors/Tissue-Separating-Scissors/14072-10	Spared nerve injury
Student Vannas Spring Scissors	Fine Science Tools	91500-09	https://www.finescience.com/en-US/Products/Scissors/Spring-Scissors/Student-Vannas-Spring-Scissors/91500-09-(1)	Spared nerve injury
Personnet Mini Retractor	Roboz	RS-6504	http://shopping.robоз.com/micro-scissors-micro-forceps-groups/Spreading/RS-6504-Personnet-Mini-Retractor-1-3X3-4mm-Sharp-Prongs	Implant (optional step)
Absorbable suture	Patterson Dental	PGA 6-0. #090-1660	https://www.pattersondental.com/Supplies/ProductFamilyDetails/PIF_537732	Implant
8-0 silk sutures	S&T	03192		Spared nerve injury
6-0 silk sutures	Henry Schein	101-2636	https://www.henryschein.com/us-en/Shopping/ProductDetails.aspx?productid=1012636&CatalogName=DENTAL	Spared nerve injury
Delicate bone scraper	Fine Science Tools	10075-16	https://www.finescience.com/en-US/Products/Bone-Instruments/Bone-Chisels/Delicate-Bone-Scraper/10075-16	Implant
Titanium Micro Spatula	Fine Science Tools	10167-11	https://www.finescience.com/en-US/Products/Spatulae,-Spoons-Curettes/Spatulae/Titanium-Micro-Spatula/10167-11	Implant
Micro drill	Foredom	K.1070	https://www.foredom.net/product/k-1070-high-speed-rotary-micromotor-kit-2-35mm-3-32-or-1-8-collet/	Laminectomy

Item	Vendor	Product No.	Website	Experiment/Note
Acu-Needle 33G – 1/2” (Needles)	Accuderm inc.	NP335	https://www.fishersci.com/shop/products/NC1145832/NC1145832	Implant
Universal Dentin Activator Gel (10% Citric acid, 3% Ferric chloride)	Parkell	S394	https://www.parkell.com/c-b-metabond_7	Implant (optional step)
3 mm coverslip (#0)	Warner Instruments	640726	https://www.warneronline.com/coverslip-coverglass	Window
1-mm borosilicate glass capillaries	WPI	1B100F-4	https://www.wpiinc.com/var-1953-standard-glass-capillaries	Intraspinal injection
PUL-100 puller	WPI	P-100		Intraspinal injection
Hamilton syringe	Hamilton	7653-01	https://www.hamiltoncompany.com/lab-oratory-products/syringes/7653-01	Intraspinal injection
Crescent blade - Micro Knife	Fine Science Tools	10317-14	https://www.finescience.com/en-US/Products/Scalpels-Blades/Micro-Knives/Micro-Knives-Plastic-Handle/10317-14	Laminectomy
Electronic Super Knips®	Knipex	7861125	https://www.knipex.com/products/electronics-pliers/electronic-super-knips/electronic-super-knips/7861125	Implant
Adhesives				
Vetbond	3M	1469SB	https://www.3m.com/3M/en_US/p/d/v00058033/	Implant
Super Glue	Loctite	1365882	https://www.loctiteproducts.com/en/products/fix/super-glue/loctite_super_glueliquidprofessional.html	Implant
Low Toxicity Silicone Adhesive	WPI	KWIK-SIL	https://www.wpiinc.com/kwik-sil-low-toxicity-silicone-adhesive?	Implant, Laminectomy, Window
C&B Metabond® Quick Adhesive Cement System PMMA (includes universal gel dentin activator)	Parkell	S380	https://www.parkell.com/c-b-metabond_3	Implant, Window
Norland Optical Adhesive NOA 81	Edmund Optics	36-428	https://www.edmundoptics.com/p/1-oz-application-bottle-of-noa-81/4179/	Window (alternative to cement)
General use				
Patterson® Disposable Micro Applicator – 0.5 mm	Patterson Dental Supply	070826198	https://www.pattersondental.com/Supplies/ItemDetail/070826198	Surgery (general use)
Weck-Cel® Cellulose Eye Spears	BVI Medical	0008680	https://www.bvimedical.com/products/fluid-control/	Surgery (general use)
UV flashlight	LIGHTFE (Amazon)	FL 365NM	https://www.amazon.com/gp/product/B07BC8L581/ref=ppx_yo_dt_b_search_asin_title?ie=UTF8&psc=1	Window (alternative to cement)
Nair™ hair removal cream	Nair	22600223191	http://www.naircare.com/en/women/products/nair-lotion-with-baby-oil	Implant
Wahl Professional Shaver	Wahl Clipper Corp	8685	https://www.wahlpro.com/shop/classic-peanut-08685	Surgery (spared nerve injury)
Press'n Seal®	Glad	Press'n Seal®	https://www.glad.com/food-storage/plastic-wrap/press-n-seal-home-collection	Surgery (general use)
SYSTANE® NIGHTTIME Eye Ointment	Alcon	02444062	https://systane.myalcon.com/eye-care/systane/products/systane-nighttime/	Surgery (general use)
Povidone Iodine Prep Solution, 4 oz.	Medline	MDS093944H	https://www.medline.com/sku/item/MDPMS093944H	Implant
Synthetics				
Teflon AF 2400 membrane	VICI Metronics	AF-050-025-025 (25mm x 25mm x 50µm)	https://www.vicimetronics.com/collections/random-technologies-teflon-af-products/products/teflon-af-films-1	Window
GORE® PRECLUDE® Pericardial Membrane	Gore Medical (acquired through Dotmed.com or other resale vendor)	1PCM101	https://www.goremedical.com/products/precludepericardial	Laminectomy
Viruses				
AAV-PHP.eB-CAG-nls-GFP	Addgene	104061-PHPeB	https://www.addgene.org/104061/	Retro-orbital injections
AAV-PHP.S-CAG-tdTomato	Addgene	59462-PHP.S	https://www.addgene.org/59462/	Retro-orbital injections
AAV2retro-hSyn-Cre	Addgene	105553-AVVrg	https://www.addgene.org/105553/	Intraspinal injection
In vivo imaging setup				

Item	Vendor	Product No.	Website	Experiment/Note
VIVO Multiphoton	3i		https://www.intelligent-imaging.com/vivo-multiphoton	
Mug Warmer Cooler	Yeosen	PH-F3		Sensory stimuli (awake)
Hot plate	Fisher Scientific	HP88854200	https://medexsupply.com/fisher-scientific-isotemp-ceramic-hotplate-4-25-x-4-25-120v-60hz/	Sensory stimuli (awake)
Glass Syringes	Synthware™	S371202	https://www.fishersci.com/shop/products/graduated-borosilicate-glass-syringes/31502318	Sensory stimuli (awake)
Brush	NicPro	MG015, Flat 1 and Round 1	https://nicpro.com/products/nicpro-micro-detail-paint-brush-set-15-tiny-professional-miniature-fine-detail-brushes-detailing-paint-kit-for-spray-watercolor-oil-acrylic-craft-models-painting	Sensory stimuli (awake)
Forceps (Pinch)	AVEN	18434	https://www.aventools.com/aven-8-forceps-wstraight-serrated-tips	Sensory stimuli (awake)
Force sensitive resistor	Adafruit	166	https://www.adafruit.com/product/166	Sensory stimuli (awake)
Compressed gas duster	Dust-off	8541677532, 8541677551		Air puff stimulus
Piezo Buzzer	Intervox	BRP3018L-12-C	https://us.rs-online.com/product/icc-intervox/brp3018l-12-c70115792/	Sound Stimulus
Low-Profile Anesthesia Mask	Kent Scientific	SOMNO-0801	https://www.kentscientific.com/products/low-profile-anesthesia-masks-for-somnosuite/	Acute imaging
Ultrasound gel	Parker Labs	638632490755 (01-34)	https://www.parkerlabs.com/products/aquasonic-100-ultrasound-transmission-gel/	Imaging
Infrared acrylic	ePlastics	ACRY31430.125PM11.555x11.850	https://www.eplastics.com/ACRY31430-125PM11-555X11-850	Mouse blinders and circular running wheel
Infrared 850 nm IR LED Strip Light	Waveform Lighting	7031.85	https://store.waveformlighting.com/products/infrared-850-nm-ir-led-strip-light	NIR imaging
Infrared Night Vision Illuminator	LIYUDL	B071KPSGCT	https://www.amazon.com/LIYUDL-48-LED-Infrared-Illuminator-Security/dp/B071KPSGCT	NIR imaging
JC Infrared Illuminator	Shenzhen Jing Cheng Digital Surveillance Co,	IRINB04L	https://www.amazon.com/Infrared-Illuminator-Power-Vision-Camera/dp/B01D73XM24	NIR imaging
Red LED Flexible Strip Ribbon Light	ALITOVE	AL5RWPBK12V	https://www.amazon.com/ALITOVE-Flexible-Waterproof-Commercial-Lighting/dp/B07MXXDWDW?th=1	LED
FilmGrade™ Flicker-Free LED Dimmer	Waveform Lighting	3081	https://store.waveformlighting.com/products/filmgrade-flicker-free-dimmer-for-led-strip?src=pse	LED dimmer
Goniometer	Thorlabs	GNL20	https://www.thorlabs.com/thorproduct.cfm?partnumber=GNL20	Setup
Jack	Thorlabs	L490	https://www.thorlabs.com/thorproduct.cfm?partnumber=L490	Setup
Mounting bracket	Thorlabs	C1515	https://www.thorlabs.com/thorproduct.cfm?partnumber=C1515	Setup
Aluminum perforated sheet	McMaster Carr	92725T51	https://www.mcmaster.com/92725T51/	Setup (circular running wheel)
Rotary encoder	Signswise	LN11-ERGA	https://www.amazon.com/Signswise-Incremental-Optical-Encoder-Quadrature/dp/B00Y9KDDCY?th=1	600 P/R
3D printed parts	Custom		https://github.com/basbaumlab/spinal_cord_imaging	Connects running wheel to the rotary encoder
3D printed part	Custom		https://github.com/basbaumlab/spinal_cord_imaging	Attaches rotary encoder to Thorlabs posts.
245mm Square Dishes	Corning	07-200-600	https://www.fishersci.com/shop/products/corning-245mm-square-bioassay-dishes-3/07200600	Setup (plastic cover)
Saleae Logic 8	Saleae	SAL-00111	https://usd.saleae.com/products/saleae-logic-8	Setup (logic analyzer)
Decibel Meter	Tadeto	SL720	https://www.amazon.com/Tadeto-Portable-Backlight-Weighted-Factories/dp/B09T37812W?th=1	Sound meter
Compact Power and Energy Meter Console	Thorlabs	PM100D	https://www.thorlabs.com/thorproduct.cfm?partnumber=PM100D	Power output for imaging

Item	Vendor	Product No.	Website	Experiment/Note
Standard Photodiode Power Sensor	Thorlabs	S120C	https://www.thorlabs.com/thorproduct.cfm?partnumber=S120C	LED power output for one-photon imaging
Standard Photodiode Power Sensor	Thorlabs	S121C	https://www.thorlabs.com/thorproduct.cfm?partnumber=S121C	Laser power output for two-photon imaging
Hirose cable	The Imaging Source	CA-x2-HIR-OE/1.5		Sync cameras with imaging
Fluorescent microspheres	Invitrogen	F8765		
Cameras for one-photon imaging				
CoolSNAP EZ	Teledyne Photometrics		https://www.photometrics.com/wp-content/uploads/2019/10/CoolSNAP-EZ-Datasheet.pdf	
Kinetix	Teledyne Photometrics		https://www.photometrics.com/products/kinetix-family/kinetix	
Fusion BT	Hamamatsu Photonics K.K.	C15440-20UP	https://www.hamamatsu.com/eu/en/product/cameras/cmos-cameras/C15440-20UP.html	
Prime BSI	Teledyne Photometrics		https://www.photometrics.com/products/prime-family/primebsi	
pco.edge 4.2 bi	Excelitas PCO GmbH		https://www.pco.de/scientific-cameras/pcoedge-42/	
Axiocam 712	Zeiss			
Behavior room				
Lamp	JOOFO	Clipper0722-54	https://www.amazon.com/JOOFO-Torchiere-Temperatures-Lamps-Tail-Office%EF%BC%88Black%EF%BC%89/dp/B07WFC14VR	Behavior (general use)
Lamp	Barrina	INWT504005650Fc	https://www.amazon.com/Barrina-Dimmable-Adjustable-3000K-5500K-Flexible/dp/B078S57SG4	Behavior (general use)
Digital Lux meter	JRLGD	LX1010B	https://drmeter.com/products/digital-lux-meter-digital-illuminance-light-meter-lx1010b-dr-meter	Behavior (general use)
Camera	The Imaging Source	DMK 21AU04, DFK 42BUC03	* https://www.theimagingsource.com/en-us/product/industrial/2u/dfk42buc03/ * https://dl-gui.theimagingsource.com/en_US/316abb0-5e27-575c-b0ef-ded415604df4/	Behavior (general use)
Touch Test™ Sensory Probes, Stoelting	Stoelting	58011	https://us.vwr.com/store/product/23125281/touch-testtm-sensory-probes-stoelting	von Frey filaments
Rotarod	Ugo Basile	7650, 47650	https://ugobasile.com/products/categories/motory-coordination/rotarod-for-mice-and-rats	Behavior (Rotarod test)
Arena 2-ft diameter, white	TAP Plastics	HDPE		Behavior (Open field)
15.5–16" tall white walls	Mr. Plastics	WHT POLYSTYRENE		Behavior (Open field)
Freely moving imaging with miniature microscopes				
nVista	Inscopix		https://inscopix.com/nvista-system/	
Miniscope V4.4	Open Ephys		https://open-ephys.org/miniscope-v4/miniscope-v4	
Miniscope DAQ v3.3	Open Ephys		https://open-ephys.org/miniscope-daqs/daq	
LScape module for nVue 2.0	Inscopix		https://inscopix.com/nvue-system	
Flow-It A2	Pentron Clinical	N11VB	https://www.pentron.com/en-us/composites/flow-it-alc-flowable-0	
Miniscope baseplate	Inscopix	1050-004638		
Miniscope V4 Base Plate [Variant 2]	Open Ephys		https://open-ephys.org/miniscope-v4/miniscope-v4-base-plate-variant-2	
UV curable glue	Loctite	4310	https://next.henkel-adhesives.com/us/en/products/industrial-adhesives/central-pdp.html/loctite-4310/BP000000379228.html	

SUPPLEMENTARY REFERENCES

1. Wall, P. D., Freeman, J. & Major, D. Dorsal horn cells in spinal and in freely moving rats. *Exp. Neurol.* **19**, 519–529 (1967).
2. Cleland, C. L. & Hoffer, J. A. Activity Patterns of Spinocerebellar Neurons during Normal Locomotion. in *Neurobiology of Vertebrate Locomotion: Proceedings of an International Symposium held at The Wenner-Gren Center, Stockholm, June 17th – 19th, 1985* (eds. Grillner, S., Stein, P. S. G., Stuart, D. G., Forssberg, H. & Herman, R. M.) 705–723 (Palgrave Macmillan UK, London, 1986).
3. Hadzipasic, M. *et al.* Reduced high-frequency motor neuron firing, EMG fractionation, and gait variability in awake walking ALS mice. *Proc. Natl. Acad. Sci. U. S. A.* **113**, E7600–E7609 (2016).
4. Kerschensteiner, M., Schwab, M. E., Lichtman, J. W. & Misgeld, T. In vivo imaging of axonal degeneration and regeneration in the injured spinal cord. *Nat. Med.* **11**, 572–577 (2005).
5. Davalos, D. *et al.* Stable in vivo imaging of densely populated glia, axons and blood vessels in the mouse spinal cord using two-photon microscopy. *J. Neurosci. Methods* **169**, 1–7 (2008).
6. Dray, C., Rougon, G. & Debarbieux, F. Quantitative analysis by in vivo imaging of the dynamics of vascular and axonal networks in injured mouse spinal cord. *Proc. Natl. Acad. Sci. U. S. A.* **106**, 9459–9464 (2009).
7. Di Maio, A. *et al.* In vivo imaging of dorsal root regeneration: rapid immobilization and presynaptic differentiation at the CNS/PNS border. *J. Neurosci.* **31**, 4569–4582 (2011).
8. Lorenzana, A. O., Lee, J. K., Mui, M., Chang, A. & Zheng, B. A surviving intact branch stabilizes remaining axon architecture after injury as revealed by in vivo imaging in the mouse spinal cord. *Neuron* **86**, 947–954 (2015).
9. Farrar, M. J. *et al.* Chronic in vivo imaging in the mouse spinal cord using an implanted chamber. *Nat. Methods* **9**, 297–302 (2012).
10. Fenrich, K. K. *et al.* Long-term in vivo imaging of normal and pathological mouse spinal cord with subcellular resolution using implanted glass windows. *J. Physiol.* **590**, 3665–3675 (2012).
11. Figley, S. A. *et al.* A spinal cord window chamber model for in vivo longitudinal multimodal optical and acoustic imaging in a murine model. *PLoS One* **8**, e58081 (2013).
12. Tang, P. *et al.* In vivo two-photon imaging of axonal dieback, blood flow, and calcium influx with methylprednisolone therapy after spinal cord injury. *Sci. Rep.* **5**, 9691 (2015).
13. Yang, Z., Xie, W., Ju, F., Khan, A. & Zhang, S. In vivo two-photon imaging reveals a role of

- progesterone in reducing axonal dieback after spinal cord injury in mice. *Neuropharmacology* **116**, 30–37 (2017).
14. Tedeschi, A. *et al.* The Calcium Channel Subunit Alpha2delta2 Suppresses Axon Regeneration in the Adult CNS. *Neuron* **92**, 419–434 (2016).
 15. Schaffran, B., Hilton, B. J. & Bradke, F. Imaging in vivo dynamics of sensory axon responses to CNS injury. *Exp. Neurol.* **317**, 110–118 (2019).
 16. El Waly, B. *et al.* Intravital Assessment of Cells Responses to Conducting Polymer-Coated Carbon Microfibres for Bridging Spinal Cord Injury. *Cells* **10**, (2021).
 17. Escarrat, V., Perez-Sanchez, J., El-Waly, B., Collazos-Castro, J. E. & Debarbieux, F. Composite Fibrin and Carbon Microfibre Implant to Modulate Postraumatic Inflammation after Spinal Cord Injury. *Cells* **12**, (2023).
 18. Farrar, M. J. & Schaffer, C. B. A procedure for implanting a spinal chamber for longitudinal in vivo imaging of the mouse spinal cord. *J. Vis. Exp.* (2014) doi:10.3791/52196.
 19. DeNotta, S. A. L. In-vivo Multiphoton Excited Fluorescence Microscopy of the Spinal Cord. (Cornell University, 2018). doi:10.7298/a1tm-z178.
 20. Laskowski, C. J. & Bradke, F. In vivo imaging: a dynamic imaging approach to study spinal cord regeneration. *Exp. Neurol.* **242**, 11–17 (2013).
 21. Cupido, A., Catalin, B., Steffens, H. & Kirchhoff, F. Surgical Procedures to Study Microglial Motility in the Brain and in the Spinal Cord by In Vivo Two-Photon Laser-Scanning Microscopy. in *Laser Scanning Microscopy and Quantitative Image Analysis of Neuronal Tissue* (eds. Bakota, L. & Brandt, R.) 37–50 (Springer New York, New York, NY, 2014).
 22. Steffens, H., Nadrigny, F. & Kirchhoff, F. Preparation of the mouse spinal column for single imaging using two-photon laser-scanning microscopy. *Cold Spring Harb. Protoc.* **2012**, (2012).
 23. Steffens, H., Nadrigny, F. & Kirchhoff, F. Preparation of the mouse spinal column for repetitive imaging using two-photon laser-scanning microscopy. *Cold Spring Harb. Protoc.* **2012**, (2012).
 24. Cartarozzi, L. P. *et al.* In vivo two-photon imaging of motoneurons and adjacent glia in the ventral spinal cord. *J. Neurosci. Methods* **299**, 8–15 (2018).
 25. Shekhtmeyster, P. Miniature Microscopy for Biological Applications. (UC San Diego, 2019).
 26. Rajaei, A., Geisen, M. E., Sellers, A. K. & Stirling, D. P. Repeat intravital imaging of the murine spinal cord reveals degenerative and reparative responses of spinal axons in real-time following a

- contusive SCI. *Exp. Neurol.* **327**, 113258 (2020).
27. Sullivan, S. J. & Sdrulla, A. D. Excitatory and Inhibitory Neurons of the Spinal Cord Superficial Dorsal Horn Diverge in Their Somatosensory Responses and Plasticity in Vivo. *J. Neurosci.* **42**, 1958–1973 (2022).
 28. Rieder, P. *et al.* Astrocytes and Microglia Exhibit Cell-Specific Ca²⁺ Signaling Dynamics in the Murine Spinal Cord. *Front. Mol. Neurosci.* **15**, 840948 (2022).
 29. Rieder, P. Glial Ca²⁺ signaling in the spinal cord and the myelin-protective effect of the GABA_B receptor in oligodendrocyte precursor cells. (Saarländische Universitäts-und Landesbibliothek, 16-Nov-2023).
 30. Yarmolinsky, D. A. *et al.* Selective modification of ascending spinal outputs in acute and neuropathic pain states. *bioRxiv* 2024.04.08.588581 (2024) doi:10.1101/2024.04.08.588581.
 31. Shekhtmeyster, P. *et al.* Trans-segmental imaging in the spinal cord of behaving mice. *Nat. Biotechnol.* (2023) doi:10.1038/s41587-023-01700-3.
 32. Shekhtmeyster, P. *et al.* Multiplex translaminar imaging in the spinal cord of behaving mice. *Nat. Commun.* **14**, 1–14 (2023).
 33. Sekiguchi, K. J. *et al.* Imaging large-scale cellular activity in spinal cord of freely behaving mice. *Nat. Commun.* **7**, 11450 (2016).
 34. Cheng, Y. T. *et al.* In-Vivo Three-Photon Excited Fluorescence Imaging in the Spinal Cord of Awake, Locomoting Mouse. in *Frontiers in Optics 2016* (2016). doi:10.1364/FIO.2016.JTh2A.183.
 35. Ju, F. *et al.* Long-term two-photon imaging of spinal cord in freely behaving mice. *bioRxiv* 2022.01.09.475306 (2022) doi:10.1101/2022.01.09.475306.
 36. Celinskis, D. Multi-site and multi-modal imaging methods for studying spinal, brain, and vascular dynamics. (Brown University, 2022).
 37. Celinskis, D. *et al.* Towards a Brighter Constellation: Multi-Organ Neuroimaging of Neural and Vascular Dynamics in the Spinal Cord and Brain. *bioRxiv* 2023.12.25.573323 (2023) doi:10.1101/2023.12.25.573323.
 38. Roina, Y., Auber, F., Hocquet, D. & Herlem, G. ePTFE-based biomedical devices: An overview of surgical efficiency. *J. Biomed. Mater. Res. B Appl. Biomater.* **110**, 302–320 (2022).
 39. Korinek, P. M. Amorphous fluoropolymers - a new generation of products. *Macromol. Symp.* **82**, 61–65 (1994).

40. Resnick, P. R. & Buck, W. H. Teflon® AF: A family of amorphous fluoropolymers with extraordinary properties. in *Topics in Applied Chemistry* (ed. Gareth Hougham, Patrick E. Cassidy, Ken Johns, Theodore Davidson) 25–33 (Kluwer Academic Publishers, Boston, 2002).
41. Rotta, J. M., Reis, R. C., de Carvalho, A. L. M. & de Oliveira, M. F. Use of an Expanded Polytetrafluoroethylene (ePTFE) Dura Substitute in Glioma Surgeries: A Technical Note. *Arquivos Brasileiros de Neurocirurgia: Brazilian Neurosurgery* **38**, 236–238 (2019).
42. Kurt, G. *et al.* Comparison of Oxiplex and Gore-Tex effectivity in an experimental peridural fibrosis model. *Neurocirurgia* **20**, 360–366 (2009).
43. Lladó, A., Guimerá, J., Garcia, F. & Navarro, A. Expanded polytetrafluoroethylene membrane for the prevention of peridural fibrosis after spinal surgery: an experimental study. *Eur. Spine J.* **8**, 138–143 (1999).
44. Loebe, M., Alexi-Meskishvili, V., Weng, Y., Hausdorf, G. & Hetzer, R. Use of polytetrafluoroethylene surgical membrane as a pericardial substitute in the correction of congenital heart defects. *Tex. Heart Inst. J.* **20**, 213–217 (1993).
45. Zehr, K. J. *et al.* Protection of the internal mammary artery pedicle with polytetrafluoroethylene membrane. *J. Card. Surg.* **8**, 650–655 (1993).
46. Koguchi, R., Jankova, K. & Tanaka, M. Fluorine-containing bio-inert polymers: Roles of intermediate water. *Acta Biomater.* **138**, 34–56 (2022).
47. Hernandez, J. L. & Woodrow, K. A. Medical Applications of Porous Biomaterials: Features of Porosity and Tissue-Specific Implications for Biocompatibility. *Adv. Healthc. Mater.* **11**, e2102087 (2022).
48. Takahashi, T. *et al.* PEO-CYTOP Fluoropolymer Nanosheets as a Novel Open-Skull Window for Imaging of the Living Mouse Brain. *iScience* **23**, 101579 (2020).
49. Takahashi, T. *et al.* Large-scale cranial window for in vivo mouse brain imaging utilizing fluoropolymer nanosheet and light-curable resin. *Commun Biol* **7**, 232 (2024).
50. Pados, G., Venetis, C. A., Almaloglou, K. & Tarlatzis, B. C. Prevention of intra-peritoneal adhesions in gynaecological surgery: theory and evidence. *Reprod. Biomed. Online* **21**, 290–303 (2010).
51. Shtoyerman, E., Arieli, A., Slovin, H., Vanzetta, I. & Grinvald, A. Long-term optical imaging and spectroscopy reveal mechanisms underlying the intrinsic signal and stability of cortical maps in V1 of behaving monkeys. *J. Neurosci.* **20**, 8111–8121 (2000).

52. Arieli, A., Grinvald, A. & Slovin, H. Dural substitute for long-term imaging of cortical activity in behaving monkeys and its clinical implications. *J. Neurosci. Methods* **114**, 119–133 (2002).
53. Chen, L. M. *et al.* A chamber and artificial dura method for long-term optical imaging in the monkey. *J. Neurosci. Methods* **113**, 41–49 (2002).
54. Ghanbari, L. *et al.* Cortex-wide neural interfacing via transparent polymer skulls. *Nat. Commun.* **10**, 1500 (2019).
55. Greenberg, D. S. & Kerr, J. N. D. Automated correction of fast motion artifacts for two-photon imaging of awake animals. *J. Neurosci. Methods* **176**, 1–15 (2009).
56. Nelson, N. A., Wang, X., Cook, D., Carey, E. M. & Nimmerjahn, A. Imaging spinal cord activity in behaving animals. *Exp. Neurol.* **320**, 112974 (2019).
57. Supekar, O. D. *et al.* Miniature structured illumination microscope for in vivo 3D imaging of brain structures with optical sectioning. *Biomed. Opt. Express* **13**, 2530–2541 (2022).
58. Neil, M. A., Juskaitis, R. & Wilson, T. Method of obtaining optical sectioning by using structured light in a conventional microscope. *Opt. Lett.* **22**, 1905–1907 (1997).
59. Chen, W. *et al.* In vivo volumetric imaging of calcium and glutamate activity at synapses with high spatiotemporal resolution. *Nat. Commun.* **12**, 6630 (2021).
60. Cheng, Y.-T. In vivo Three-Photon Excited Fluorescence Functional Imaging of the Spinal Cord in Health and Disease. (Cornell University, Ann Arbor, United States, 2020).
61. Icha, J., Weber, M., Waters, J. C. & Norden, C. Phototoxicity in live fluorescence microscopy, and how to avoid it. *Bioessays* **39**, (2017).
62. Donnert, G., Eggeling, C. & Hell, S. W. Major signal increase in fluorescence microscopy through dark-state relaxation. *Nat. Methods* **4**, 81–86 (2007).
63. Larsch, J., Ventimiglia, D., Bargmann, C. I. & Albrecht, D. R. High-throughput imaging of neuronal activity in *Caenorhabditis elegans*. *Proc. Natl. Acad. Sci. U. S. A.* **110**, E4266-73 (2013).
64. Boudreau, C. *et al.* Excitation Light Dose Engineering to Reduce Photo-bleaching and Photo-toxicity. *Sci. Rep.* **6**, 30892 (2016).
65. Penjweini, R., Loew, H. G., Hamblin, M. R. & Kratky, K. W. Long-term monitoring of live cell proliferation in presence of PVP-Hypericin: a new strategy using ms pulses of LED and the fluorescent dye CFSE. *J. Microsc.* **245**, 100–108 (2012).
66. Nishigaki, T., Wood, C. D., Shiba, K., Baba, S. A. & Darszon, A. Stroboscopic illumination using

- light-emitting diodes reduces phototoxicity in fluorescence cell imaging. *Biotechniques* **41**, 191–197 (2006).
67. Hendrix, J., Flors, C., Dedecker, P., Hofkens, J. & Engelborghs, Y. Dark states in monomeric red fluorescent proteins studied by fluorescence correlation and single molecule spectroscopy. *Biophys. J.* **94**, 4103–4113 (2008).
68. Ludvikova, L. *et al.* Near-infrared co-illumination of fluorescent proteins reduces photobleaching and phototoxicity. *Nat. Biotechnol.* (2023) doi:10.1038/s41587-023-01893-7.
69. Hoebe, R. A. *et al.* Controlled light-exposure microscopy reduces photobleaching and phototoxicity in fluorescence live-cell imaging. *Nat. Biotechnol.* **25**, 249–253 (2007).
70. Grewe, B. F., Langer, D., Kasper, H., Kampa, B. M. & Helmchen, F. High-speed in vivo calcium imaging reveals neuronal network activity with near-millisecond precision. *Nat. Methods* **7**, 399–405 (2010).
71. Griffiths, V. A. *et al.* Real-time 3D movement correction for two-photon imaging in behaving animals. *Nat. Methods* **17**, 741–748 (2020).
72. Nath, T. *et al.* Using DeepLabCut for 3D markerless pose estimation across species and behaviors. *Nat. Protoc.* **14**, 2152–2176 (2019).